Pulsating Downslope Windstorms

J. F. SCINOCCA AND W. R. PELTIER

Department of Physics, University of Toronto, Toronto, Ontario, Canada

(Manuscript received 29 September 1988, in final form 28 April 1989)

ABSTRACT

The flow configurations that obtain in several severe downslope windstorm events generated over isolated topography are studied using a two-dimensional nonlinear anelastic model. A new high resolution simulation of the 11 January 1972 windstorm in Boulder, Colorado, constructed using a very large model domain, is shown to qualitatively reproduce the strong, quasi-periodic, 5–15 min transience in surface wind speed to the lee of the topography that was actually observed during this event. It is demonstrated that this transience is caused by the continuous generation of strong pulses of enhanced surface wind on the lee slope, which thereafter propagate downstream with individually constant speeds. An identical phenomenon is shown to be characteristic of the high drag regime in severe downslope windstorms simulated in flows characterized by upstream profiles having constant wind and stability. This newly discovered pulsation phenomenon is therefore a generic property of flows induced by the breaking of topographically forced internal waves.

1. Introduction

The past decade has witnessed the expenditure of a great deal of effort in the course of attempts to unravel the detailed physical processes underlying the occurrence of severe downslope windstorms. Of particular interest has been the examination of flows possessing upstream conditions of uniform wind and stability incident upon isolated two-dimensional topography. From analyses of such flows based upon the use of fully nonhydrostatic nonlinear time-dependent numerical models (Peltier and Clark 1979, 1983; Clark and Peltier 1984; Laprise and Peltier 1989b) an inherently nonlinear mechanism has been discovered that explains the bifurcation of the flow away from the steady state solution determined analytically by Long (1953), into a strikingly different time-dependent state characterized by extremely high surface wave drag and downslope wind speed. According to the theory that has been developed to explain this phenomenon based upon the numerical simulations, incident flows that lead to the "breaking" of topographically forced internal waves necessarily undergo transformation into a new high drag state through a resonant amplification of wave energy in the cavity formed between the super adiabatic region of breaking and the ground (Peltier and Clark 1979).

This theory has received very strong recent support from the results of detailed analyses of the stability of Long's finite amplitude solution (Laprise and Peltier 1989a) which have shown that the wave field becomes unstable to a deep resonant mode of instability just as streamlines overturn and wave breaking begins. From the observed temporal evolution of the Reynolds stress profiles subsequent to breaking (Peltier and Clark 1983), it was demonstrated that only the internal wave energy in excess of that necessary to maintain critical steepness of the streamlines was coherently reflected and consequently amplified. These simple constant N (upstream profile of Brunt–Väisälä frequency) and U (upstream profile of horizontal velocity) flows have also allowed analytic steady state models to be constructed (Smith 1985) that seek, with limited success, to account for the final form of the flow in the high drag state by way of analogy with hydraulic theory (Yih 1965; Long 1970).

While such constant N and U background states have been shown to support the basic physical process by which a flow evolves into the high drag state, they seem to have limitations in their ability to deliver flows in this regime that exhibit many of the most pronounced characteristics of actual downslope windstorms. One particular example of such events that has received a great deal of attention, because of the wealth of observational data that has been collected to describe it (Lilly and Zipser 1972; Lilly 1978), is the 11 January 1972 windstorm that occurred over Boulder, Colorado. Figure 1, which will be the focus for analyses to be discussed in this paper, provides an anemometer trace reproduced from Klemp and Lilly (1975) that was recorded at the surface in the lee of the Rocky Mountains during this storm. Inspection of this figure shows that transcience in the surface wind speed occurs on three distinct time scales. An envelope comprised of a slow growth and subsequent decay is observed to occur on

Corresponding author address: Dr. W. R. Peltier, Department of Physics, University of Toronto, Toronto, Ontario, Canada M5S 1A7.

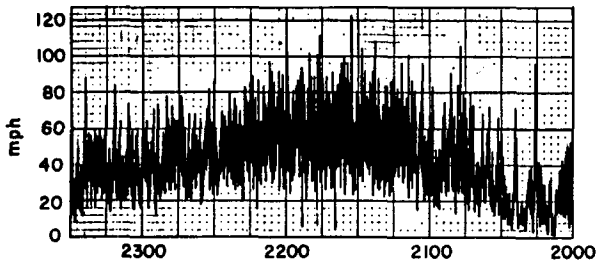

FIG. 1. Anemometer trace for the 11 January 1972 downslope windstorm in Boulder, Colorado from 2000 to 2330 (right to left) (Klemp and Lilly 1975).

the high drag configuration. As will be shown in a a time scale of O(3 h). Riding on this slowly varying background is a low frequency 5–15 minute quasi-periodic fluctuation in surface wind. On an even shorter time scale, very strong high frequency gusts appear, which occur with a period of O(1 min). In more recent observational studies, Neiman et al. (1988) have employed a pulsed doppler lidar to investigate the detailed nature of the surface wind transience that develops during downslope windstorms. During the moderate event that occurred 29 January 1987 over the Continental Divide they observed the propagation of quasi-periodic gusts in surface wind with characteristic time scales of 4–5 min and 14 min (Neiman et al., Figs. 13, 14, and 18). Further, these gusts "maintained their identity in range and time." Previous two-dimensional simulations of such severe storms generated in uniform N and U backgrounds (Peltier and Clark 1983; Durran 1986; Bacmeister and Pierrehumbert 1988), have consistently failed to provide any satisfactory explanation for the appearance of this characteristic unsteadiness that is inevitably found to accompany actual downslope windstorm events.

Several previous two-dimensional nonhydrostatic simulations have attempted to provide a detailed explanation of the 1972 Boulder storm (Peltier and Clark 1979; Durran and Klemp 1983; Durran 1986: hereafter PC79, DK83 and D86, respectively). While the transience in surface wind speed documented in Fig. 1 was never delivered by any of the above cited calculations, neither has this transience previously been the subject of any sustained inquiry. The primary purpose of these prior analyses was to investigate the factors affecting the wave breaking mechanism by which the storm initially develops. Furthermore, all of the integrations that the previously cited papers documented were teminated at or before the time that surface wave drag saturation occurred. This being the case, very little analysis of the nature of the high drag state characteristic of the mature windstorm was possible. On the basis of the domain expansion experiments, to be described in section 2 of this paper, it will be apparent that neither the horizontal nor the vertical extents of these earlier models were sufficient to allow the model to accurately describe the evolution of the flow into, and the detailed nature of, companion paper to follow, in order to understand the origin of the low frequency transience in wind speed evident on Fig. 1, the flow configuration characteristic of the high drag state must be investigated in some detail.

The only previous investigation of the surface gustiness observed during strong downslope windstorm events is that reported by Clark and Farley (1984, hereafter CF84). Based upon a combination of two- and three-dimensional model simulations, these authors advanced a theory for the 5–15 min fluctuations of horizontal wind speed revealed on the anemometer trace of Fig. 1 for the 11 January 1972 windstorm. Clearly, their work was founded on the belief that the flow in the two-dimensional downslope windstorm configuration is dynamically stable. Working from this assumption, CF84 initiated a three-dimensional simulation to determine "whether or not the two-dimensional calculations are dynamically stable with respect to perturbations in the cross-stream direction." In this study a two-dimensional ridge was employed in the three-dimensional simulation so that "one could in principle obtain identical solutions with the two- and three-dimensional models, providing the two dimensional solutions were dynamically stable." The 5–15 min quasi-periodic transience, whose initial onset they noted in their three-dimensional simulation, was therefore believed to be the result of a three-dimensional instability of the two-dimensional background state and they explicitly invoked the idea of shear aligned convective instability to rationalize its appearance—an idea that had been developed earlier by Peltier et al. (1978) and Klaassen and Peltier (1985) in the context of work on the turbulence transition in nonlinear Kelvin–Helmholtz waves. It is important to realize that, to a certain degree, the validity of the Clark and Farley conclusion depends upon the validity of their initial assumption that two-dimensional simulations delivered no such oscillation—an assumption that was never validated by any explicit comparison of their equivalent two- and three-dimensional computations.

It is reasonable, therefore, to consider what the implications might be if their initial assumption were false. If the two-dimensional flow in the fully developed downslope windstorm configuration is itself dynamically unstable, then the results obtained in CF84 become more difficult to interpret. Further, if such two-dimensional instability of itself fully embodies the 5–15 min quasi-periodic gusts of surface wind observed in the CF84 three-dimensional simulation then it would appear that the physical process responsible for this phenomenon in each case could be identical. It is apparent, therefore, that the stability of the downslope windstorm flow in two spatial dimensions must be ascertained in order to more clearly understand the dynamical origins of such surface transience.

It is the main contention of this paper that such

downslope windstorm configurations are in fact dynamically unstable in two spatial dimensions and, more importantly, that the generation of the strong 5–15 min quasi-periodic transience observed in the 11 January 1972 windstorm (and by extension all similar events) is in fact an intrinsically two-dimensional phenomenon. Based upon a large number of very long time integrations employing a variety of incident flows it will be shown here that whenever a downslope windstorm is generated through the Peltier–Clark wave breaking mechanism in two spatial dimensions, then so too is a transience in surface wind speed to the lee of the topography. Moreover, this transience is consistently manifested as a series of pulses of high velocity that each propagate downstream with a fixed phase speed in the region between the lee slope of the topography (where they appear at the surface) and the more slowly propagating Chinook front itself (in which they usually dissipate). The ability of the numerical model to deliver reliable results for very long time integrations turns out to be of paramount importance to this discovery, as we will also show, since the most intense pulses appear only after the storm has evolved into the mature high drag state.

A brief description is provided in section 2 of the fully nonhydrostatic anelastic finite difference model of Clark (1977) that has been used to perform the numerical integrations that we shall discuss. This is the same model that has been previously employed by Peltier and Clark to analyze the wave breaking process itself. In this section results will also be presented from a series of domain expansion calculations on the basis of which an appropriate model domain was selected for the lengthy time integrations. Also in this section, the nonlinear model is tested through its ability to reproduce the strong lee-wave signal that is supported by the upstream profiles that obtained during the 11 January 1972 event. This is undertaken in the linear regime with reduced mountain height so that comparison can be made with a calculation previously performed using the linear model presented in Simard and Peltier (1982).

In section 3 the main results of this inquiry are presented. Of the many incident flows studied, three of particular interest are described in detail. The first involves a reexamination of the 11 January 1972 Boulder, Colorado storm but with the two dimensional numerical integration extended to extremely long times. It is found that the mature storm delivers a strong transience of surface wind that quite closely matches the 5–15 min oscillatory structure observed in Fig. 1. This discovery prompts us to reanalyze the windstorms generated in simpler constant N and U basic states in order to test the extent to which this transient behavior is also characteristic of the severe storms induced by wave breaking in these cases. It is thereby revealed that even for such simple incident flows a windstorm transience is produced of a qualitatively similar nature to that found for the 11 January event.

In a third calculation we consider modifications to the observed upstream profiles that obtained during the 11 January 1972 Boulder, Colorado storm in an effort to assess the effect on the transient component of the response associated with relatively minor modifications of the incident flow. Also presented in section 3 is an investigation of the influence of the degree of supercriticality with respect to wave breaking and of the effect of in situ $2\Delta x$ horizontal spatial filtering on the nature and the development of the transient component of the flow. In section 4 we conclude with a brief summary of the most important results presented in the main body of the paper.

2. The nonlinear time dependent numerical model

a. Model description

Only a brief description of the two dimensional numerical model to be employed for the simulations discussed in this paper will be provided here since much of the detail can be found in Clark (1977). Sound waves are filtered from the model by rewriting the hydrodynamic field equations using the anelastic approximation. The resulting equations of continuity, conservation of momentum, and energy are, respectively:

$$\nabla \cdot (\bar{\rho}\mathbf{u}) = 0 \tag{1.a}$$

$$\bar{\rho}\frac{d\mathbf{u}}{dt} = -\nabla p' + \rho'\mathbf{g} + \nabla \cdot \tau \tag{1.b}$$

$$\bar{\rho}\frac{d\theta}{dt} = \nabla \cdot \mathbf{H}. \tag{1.c}$$

In the derivation of (1) the variables $\psi = (\rho, P, T, U, \theta)$ were expanded by the prescription $\psi(x, z, t) = \bar{\psi}(z) + \psi'(x, z, t)$ where the overbar denotes a background state, restricted to vary only in the vertical, while the primed variables represent the time dependent deviations from this basic state. The τ_{ij} are components of the symmetric stress tensor

$$\tau_{ij} = \bar{\rho} K_M D_{ij}, \tag{2}$$

in which D_{ij} is the deformation tensor

$$D_{ij} = \left(\frac{\partial u_i}{\partial x_j} + \frac{\partial u_j}{\partial x_i} - \frac{2}{3}\delta_{ij}\frac{\partial u_k}{\partial x_k}\right), \tag{3}$$

and K_M, the eddy mixing coefficient for momentum, is specified by

$$K_M = \begin{cases} (k\Delta)^2 |\mathrm{def}|(1 - \mathrm{Ri})^{1/2}, & \mathrm{Ri} < 1 \\ 0, & \mathrm{Ri} \geqslant 1. \end{cases} \tag{4}$$

In (4) k is a numerical constant, $\Delta = (\Delta x \cdot \Delta z)^{1/2}$ is a

measure of the grid resolution, Ri is the local gradient Richardson number,

$$\mathrm{Ri} = \left(g\frac{d\ln\theta}{dz}\right)\Big/(\mathrm{def})^2 \tag{5}$$

and in two spatial dimensions,

$$(\mathrm{def})^2 = \tfrac{1}{2}(D_{11}^2 + D_{22}^2) + D_{12}^2. \tag{6}$$

This crude first-order closure for the turbulent diffusion seeks to parameterize turbulent eddy mixing on the subgrid scale by enhancing viscous dissipation where the motion becomes sufficiently complicated that the scale of the grid can no longer resolve the nature of the flow. The turbulent heat flux vector **H** is represented by:

$$\mathbf{H} = \bar{\rho}K_H\nabla\theta, \tag{7}$$

and an eddy Prandtl number $\mathrm{Pr} = K_M/K_H = 1$ is assumed.

The model equations are solved in terrain following coordinates specified by the transformation (Gal-Chen and Sommerville 1975):

$$\bar{x} = x$$

$$\bar{z} = H\frac{(z - Z_s(x))}{(H - Z_s(x))}, \tag{8}$$

where the transformed coordinates are denoted by overbars, $Z_s(x)$ is the topography, and H is the height of the model domain. The Jacobian of this transformation is always nonzero so that the map is 1:1, and is given by

$$G^{1/2} = 1 - \frac{Z_s(x)}{H}. \tag{9}$$

The numerical formulation of the transformed equations (1) is based upon the use of second-order accurate centered finite differences on a staggered grid (Harlow and Welch 1965). A leapfrog scheme is employed to step the equations in time and, unless otherwise stated, the integrations are restarted every $20\Delta t$ to prevent time splitting. A Robert–Asselin running time filter (Robert 1966; Asselin 1972) is applied with a damping factor of 0.2 to all of the simulations described in what follows. Additional spatial filters constructed so as to selectively suppress $2\Delta x$ noise will also be applied in one set of calculations in order to assess the importance of this part of the wavenumber spectrum for the main physical results that we shall otherwise obtain.

In Fig. 2 a schematic illustration of the model domain is presented. At the outflow boundary, reflections have been suppressed through use of an open boundary condition based on a scheme described by Orlanski (1976). A region of Rayleigh friction is smoothly turned on well above the topography and brought to a maximum near the upper boundary. The absorption of vertically propagating wave energy affected by this region of enhanced friction serves the purpose of sim-

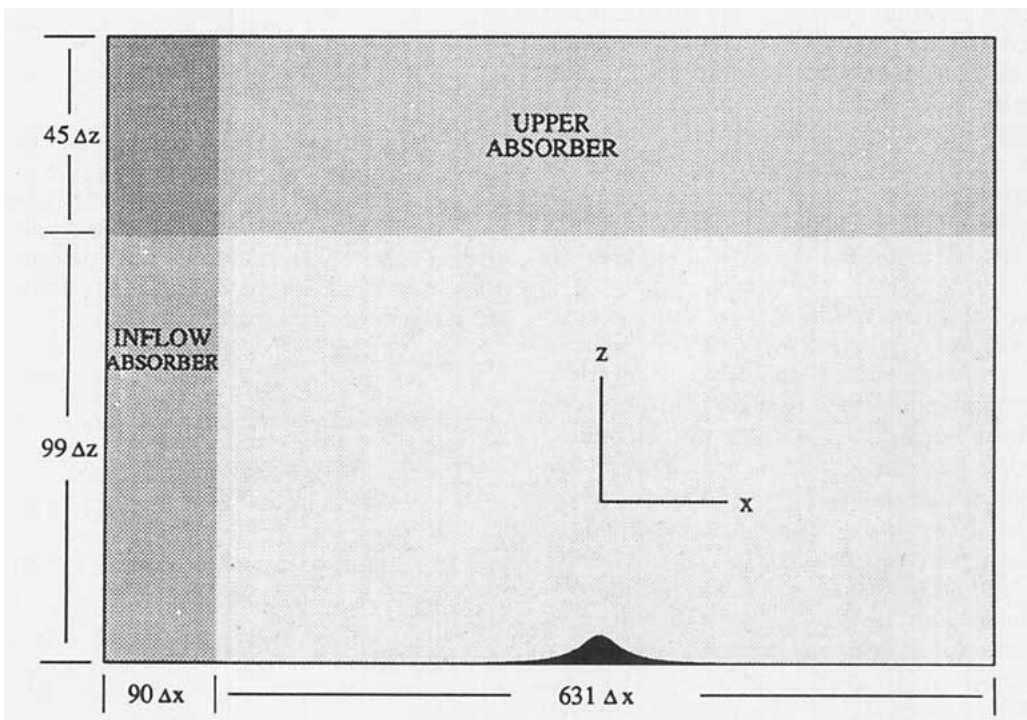

FIG. 2. The model domain.

ulating an upper radiation boundary condition and thus preventing contamination of the domain by reflection from the lid. A similar absorbing region was installed upstream. This region served to maintain the integrity of the upstream profiles throughout the integration.

The model topography employed in all calculations to be presented here is the bell-shaped profile:

$$Z_s(x) = \frac{ha^2}{x^2 + a^2}, \qquad (10)$$

where h is the mountain height and a its half-width.

b. Domain expansion calculations

Before beginning a discussion of the main group of simulations it is important in advance to understand and take great pains to limit the influence of domain size on temporally extended computations of the development and structure of the high drag configurations. The problem is that even though numerical techniques are employed to limit reflections from the lateral and overhead boundaries, these techniques are imperfect and must be assisted by moving the boundaries sufficiently far away so that on the time scales of interest the contamination is minimized.

The surface wave drag, defined as

$$D_w(t) = \int_{-\infty}^{+\infty} p\,(\bar{z} = 0, t)\left[\frac{\partial Z_s(x)}{\partial x}\right]dx,$$

was employed to gauge the sensitivity of the solution to successive independent horizontal and vertical expansions of the model domain. In these experiments, the vertical and horizontal extents of the model domain were considered adequate if the surface wave drag was self-consistent over the whole range of the temporal integration when further expansions were performed. A series of calculations were initiated with identical upstream profiles of wind and stability and fixed topography. The profiles that were employed will be discussed more fully in section 3c (Fig. 14) and, when forced with topography of the form (10), give rise to a downslope windstorm whose nature is almost identical to that which obtains in the simulation of the 11 January 1972 Boulder windstorm presented in section 3a of this paper. For these initial experiments the topography was located at the center of the horizontal range of the domain and characterized by $h \approx 2$ km and $a = 10$ km. Horizontal spatial filters (CF84) of modest strength were employed. The upper level sponge layer was held fixed at a depth of $36\Delta z$ and no upstream absorber was inserted. Vertical and horizontal resolutions of $\Delta z = 0.341$ km and $\Delta x = 0.5$ km were chosen to correspond to the highest resolution previously used for analysis of this particular problem (PC79). Table 1 contains a synopsis of the parameters employed for the domain expansion calculations along with those for several previously published simulations of the 11 January storm for comparison. Figure 3 displays a set of surface wave drag histories for a selection of these experiments.

Inspection of Fig. 3 shows that all of the drag curves appear to be very similar up to about 80 min of elapsed time when wave breaking begins above the topography. The initial domain, 181 km wide and 28.6 km high ($362\Delta x \times 84\Delta z$), is representative of the domain widths and depths employed in PC79, DK83 and D86. For this simulation a slow growth in wave drag develops after 80 min which reaches a level of 2.0×10^6 kg s^{-2} by 200 min (curve 1 of Fig. 3a). When the domain is expanded horizontally by $120\Delta x$, the drag is observed to decrease after 120 min of elapsed time and then to level off at a value of 1.0×10^6 kg s^{-2} (curve 2 of Fig. 3a). If the domain is instead increased in the vertical by $25\Delta z$, the drag is seen to grow dramatically, eventually reaching a peak value near 3.25×10^6 kg s^{-2} (curve 3 of Fig. 3a). This striking divergence of surface wave drag histories makes clear the fact that domains of even these rather significant scales are inadequate to represent accurately (which is to say eliminate the contamination by "edge effects" of) the evolution of the flow subsequent to wave breaking.

The remaining surface wave drag histories in Fig. 3a (curves 4, 5 and 6) display the effects of three successive horizontal expansions of the model domain beyond the scale of $362\Delta x \times 109\Delta z$ (curve 3 of Fig. 3a). In the first of these expansions the domain was increased by $120\Delta x$ in the horizontal. Consistent wave drag histories (curves 3 and 4) result up to a model time of 100 min. Thereafter, however, the two histories begin to diverge with the larger domain obtaining a significantly lower drag from 100–200 min. In the next expansion the domain was further increased by $160\Delta x$. This expansion produces surface wave drag histories (curves 4 and 5) that are consistent up to a model time of approximately 110 min. Beyond this time the surface wave drag histories again diverge and in this case the larger domain maintains a consistently higher level of drag (curve 5 compared to 4). In the third expansion, the model domain was again increased horizontally by $160\Delta x$. Inspection of Fig. 3a reveals that this final expansion has resulted in convergent surface wave drag histories (curves 5 and 6) insofar as the gross behavior is concerned. The detailed form of the variability, though, is never reproducible, presumably because it is associated with chaotic dynamical effects. Therefore, for a domain of this vertical scale, accurate investigation of this flow in the regime of high drag requires a domain with a minimum horizontal extent of $642\Delta x$.

In Fig. 3b is displayed a series of surface wave drag histories resulting from much longer time integrations designed to investigate the sensitivity of the simulation to the vertical extent of the model domain. For comparative purposes, the complete convergent drag histories (curves 5 and 6) of Fig. 3a are reproduced in

TABLE 1. A synopsis of the parameters which characterize previously published numerical simulations of the 11 January 1972 Boulder event as well as those employed for the domain expansion experiment described in section 2b of this paper. Eight of the simulations from this experiment are labeled (1–8) and refer to the eight drag curves presented in Fig. 3 of this paper.

Source	N	M	Domain $N\cdot\Delta x\cdot M\cdot\Delta z$ (km)				Integration time (sec)
			Δx	Δz	$N\cdot\Delta x$	$M\cdot\Delta z$	
Peltier and Clark (1979)	256	84	0.5	0.341	128.0	28.6	8 000
Durran and Klemp (1983)	128	83	1.0	0.341	128.0	28.3	8 000
Clark and Farley (1984)							
CON	242	82	1.0	0.4	242.0	32.8	4 800
CM2D	122	42	2.0	0.8	242.0	33.6	9 300
FM2D	122	42	1.0	0.4			9 300
CM3D	122	42	2.0	0.8	242.0	33.6	9 300
y dimension		12	1.0				
FM3D	122	42	1.0	0.4			9 300
y dimension		12	1.0				
Hoinka (1985)*	81	41	5.0	0.5	405.0	20.5	32 400
Durran (1986)	180	44	1.0	0.341	180.0	15.0	12 000
This paper							
1	362	84	0.5	0.341	181.0	28.6	12 000
2	482	84	0.5	0.341	241.0	28.6	11 550
3	362	109	0.5	0.341	181.0	37.2	11 500
	362	134	0.5	0.341	181.0	45.7	10 800
4	482	109	0.5	0.341	241.0	37.2	12 000
5	642	109	0.5	0.341	321.0	37.2	23 600
6	802	109	0.5	0.341	401.0	37.2	13 000
7	642	134	0.5	0.341	321.0	45.7	26 400
Final domain							
8	722	144	0.5	0.341	361.0	49.1	20 640

* Hydrostatic model.

Fig. 3b. A vertical expansion of $25\Delta z$ was initiated on the domain of scale $642\Delta x \times 109\Delta z$. The surface wave drag histories (curves 5 and 7a) appear to diverge at a model time of 125 min. These temporally extended surface wave drag histories, however, reveal that this divergence eventually disappears and that near 250 min of model time the surface wave drags converge at a level near 3.25×10^6 kg s^{-2}.

The strength of this local region of divergence in the temporal history of the surface wave drag was found to correlate well with the elevation at which the overhead absorber onsets. This tendency is clearly displayed by a comparison of the surface wave drag of simulation 7a with that of 7b. These two simulations differ only in the depth of the overhead absorber. The surface wave drag history 7b, representative of a domain for which the overhead absorber was doubled from 36 to 72 grid points, reveals a severe reduction in drag over the same temporal range of 125–250 min. This test suggests that, for domains of this scale, the local depression in the surface wave drag history described above is primarily due to transient reflections incurred at elevations in the domain where the overhead absorber turns on above the topography. It is important to note, however, that the complete drag histories displayed in Fig. 3b (curves 5, 7a, 7b) suggest that the final state achieved by the flow is relatively insensitive to the strength of the transient contamination experienced during this 125–250 min period of the simulation.

In order to model the flow more accurately during this phase of the simulation, the overhead absorber employed in the previous analyses was modified. The absorber was more smoothly introduced in the vertical by prescribing a $\sin^2$ rather than an essentially linear profile of absorber strength over its entire depth. To ensure that, at any elevation, the strength of this absorber was always less than that which would obtain with the previous design, the depth of the absorber was increased to $45\Delta z$ by vertically expanding the model domain to $144\Delta z$. An additional $80\Delta x$ grid points were added to the upstream edge of the $642\Delta x$ model domain to form the majority of a $90\Delta x$ absorber at the inflow boundary. This sponge was employed to eliminate edge effect structure at the upstream boundary which began to appear at late model times in the lengthy integrations (presumably associated with weak upstream influence). The surface wave drag for the simulation employing this domain is presented on Fig. 3b (curve 8) and will be discussed later in section 3c of this paper. All of the calculations to be reported in

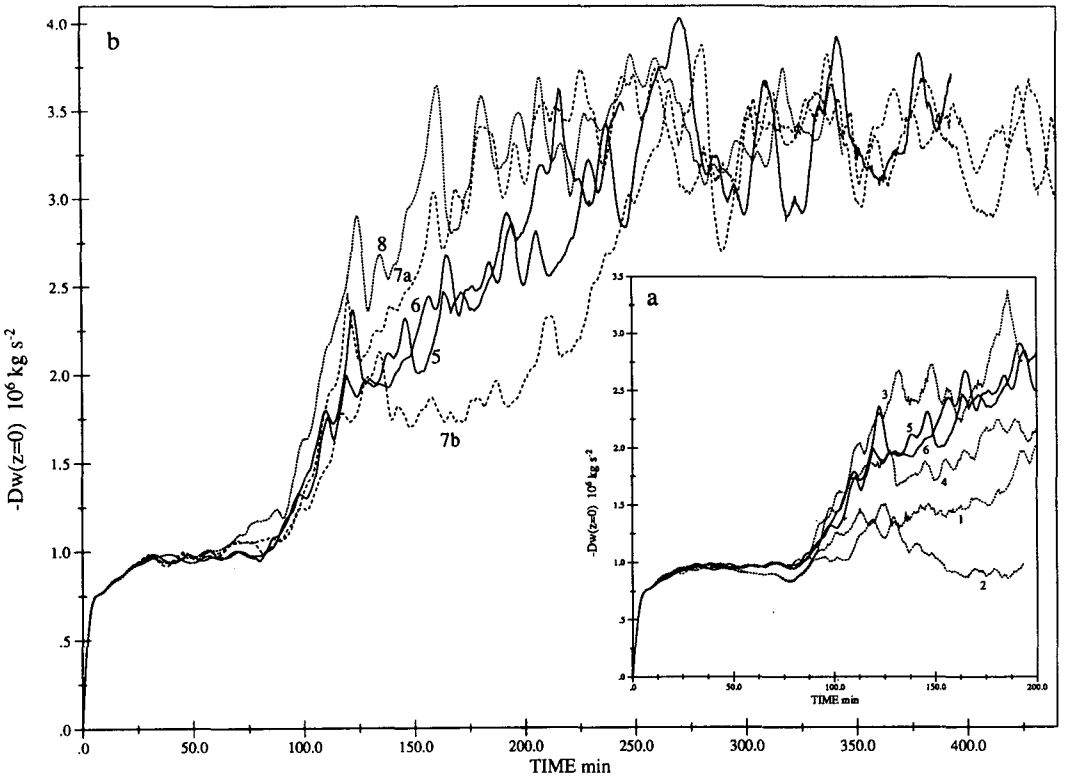

FIG. 3. Surface wave drag histories for the domain expansion experiments listed in Table 1. (a) (inset) Curves 2 and 3 respectively represent the effects of horizontal and vertical expansions beyond a domain of scale usually employed in such simulations (curve 1). Curves 4, 5, and 6 represent the effects of successive horizontal expansions of the model domain beyond the scale responsible for curve 3. (b) Surface wave drag histories from much longer temporal intergrations designed to select an appropriate vertical scale of the model domain are displayed. The local depression in surface wave drag observed to occur during the period of 125–250 min was found to be associated with spurious reflections incurred in that region of the model domain where the overhead absorber onsets.

section 3 were performed on this expanded domain and, unless otherwise specified, with Δx and Δz fixed to the above stated values and with no horizontal spatial filtering employed.

It is important to realize that the results obtained from the domain expansion experiments described above are particular to the model employed, and to the flow studied in this paper. To our knowledge a systematic study such as this has never previously been employed in the selection of a model domain for simulations of this nature. An even more thorough study than that presented here would have been preferable (e.g., a further vertical expansion beyond the scale of the final model domain). To do this, however, simulations of even greater scale would need to be performed—simulations whose cost and resource requirements would quickly become prohibitive.

c. *A linear test of the time-dependent model*

The validity of the time-dependent numerical model in the linear regime was investigated through its ability to reproduce a strong lee wave signal. Figure 4 displays the upstream profiles of wind, temperature, stability and gradient Richardson number for the 11 January 1972 windstorm in Boulder that were used as the incident flow for this test. A steady state linear model described in Simard and Peltier (1982) has previously been employed to analyze this background state with a reduced mountain height of h = 500 m and half-width a = 10 km. For comparison purposes, we have increased the stratospheric asymptotic wind speed from 20 m s^{-1} to 30 m s^{-1} for this linear test. Results from the linear calculation (Simard and Peltier 1982) demonstrated the existence of a strong lee wave mode with a wavelength of λ_x = 17.8 km.

The nonlinear time integration was initiated as inviscid and non-heat conducting and performed on the extended domain. Figure 5 presents, after 430 simulated minutes of integration, the horizontal and vertical velocities, potential temperature, and wavenumber spectra for the vertical velocity in the lee of the topography at three elevations. At this time, a strong lee wave signal pervades the three fields. Two very well defined wavelengths of the lee wave train can be seen downstream of the topography. In Fig. 5d the wave-

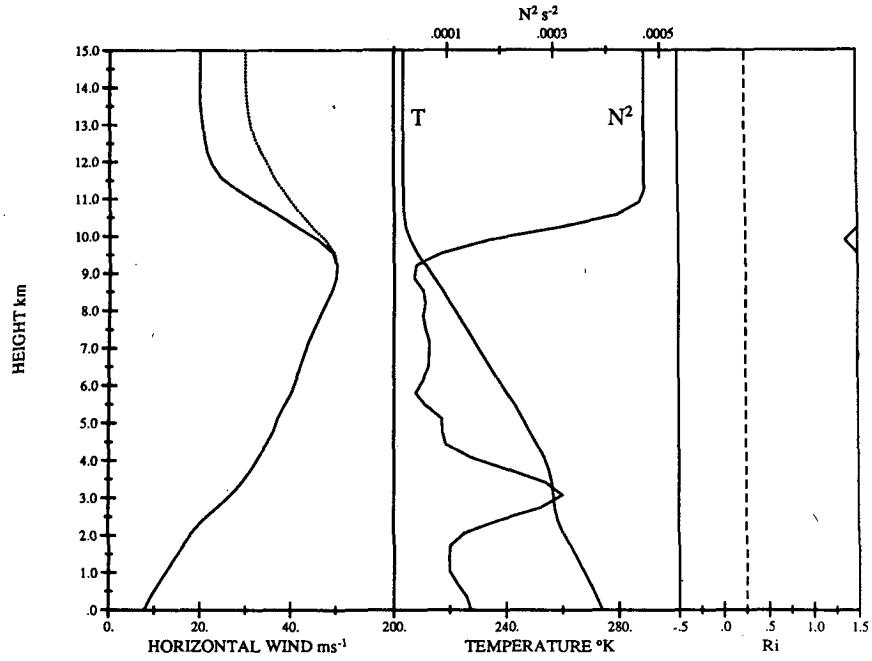

FIG. 4. Upstream profiles observed for the 11 January 1972 downslope windstorm that occurred in Boulder, Colorado (solid) and modified velocity profile employed in the lee wave simulation of section 2c (dotted).

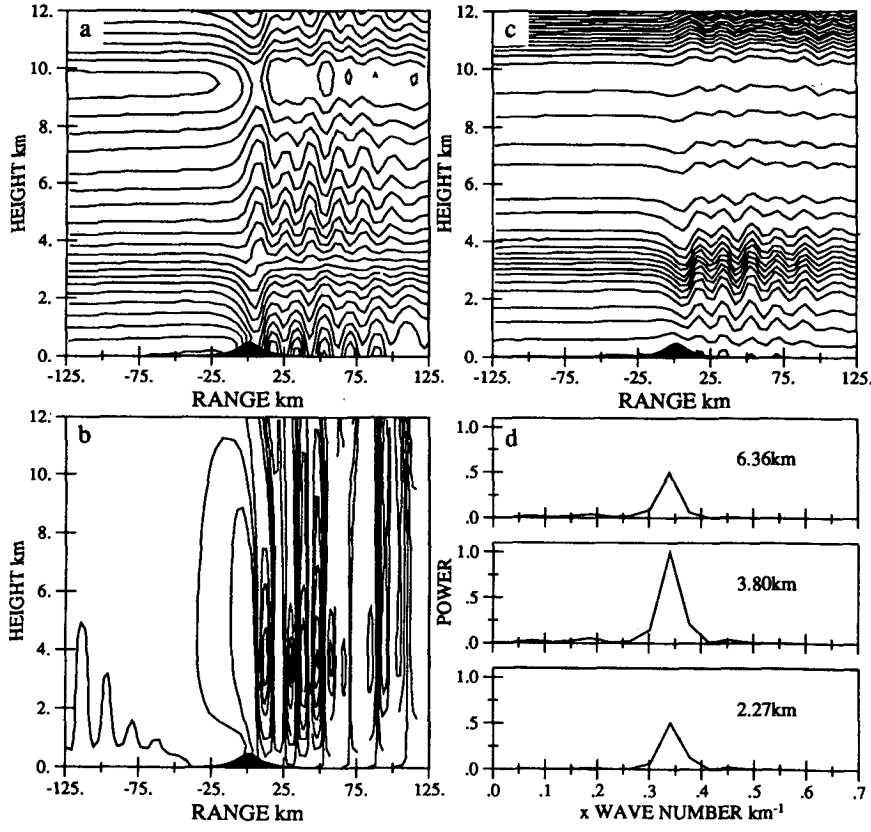

FIG. 5. Contour plots of (a) horizontal velocity, (b) vertical velocity, (c) potential temperature and (d) horizontal wave number spectra of vertical velocity to the lee of the topography at various heights in the model domain after 430 min of model time for the lee wave simulation of section 2c.

number spectra, displayed at three elevations where a significant lee wave signal was present, reveal that the wavelength of the resonance is $\lambda_x = 18.2$ km. This calculation therefore produces a lee wave mode with a wavelength within 3% of that predicted by the linear model. The nonlinear model's ability to generate a steady state in such close agreement with linear theory, further underlines the capability with the expanded domain of producing credible results for long time integrations.

3. The time-dependent nonlinear numerical calculations

In this section we shall present several nonlinear numerical simulations of downslope windstorms in two spatial dimensions in an effort to determine the nature of the transience in surface wind to the lee of the topographic maximum that develops under such ideal conditions. The primary purpose of these simulations is to establish the existence and nature of this transience, isolate the features of the flow responsible for its occurrence, and identify the factors to which the parameters that characterize it are sensitive.

a. A reexamination of the 11 January 1972 Boulder, Colorado windstorm

The first new nonlinear simulation that we will present is that for the 11 January 1972 Boulder windstorm. The well-known upstream soundings of horizontal velocity and temperature were shown previously in Fig. 4. The new integrations were performed on the extended domain described in section 2 and employed an initial time step of $\Delta t = 4$ s which was reduced to $\Delta t = 2$ s late in the high drag regime. Plotted in Fig. 6 is the surface wave drag history. Evident is the characteristic effect of the breaking event which onsets at approximately 75 min and leads to a subsequent, steep, sixfold increase in wave drag over the next 100 min of simulated time. Also marked on this figure are the times at which the previous simulations of this storm by Peltier and Clark (1979) and by Clark and Farley (1984) were terminated.

The ability of the model with the expanded domain to deliver reliable results for such long integration times, exceeding those of previous simulations by a factor of 2 (PC79; DK83; CF84; D86), leads to further insight. It is now clear that the growth in wave drag subsequent to breaking does not continue unabated. Rather, at approximately 100 min after the onset of wave breaking, the drag curve saturates at a level near 3.25×10^6 kg s^{-2}. Also, transient fluctuations in the surface wave drag appear following the onset of breaking and these grow in amplitude until the time that the surface wave drag saturates. These fluctuations in surface wave drag are a direct result, and a clear indication, of transience in the time dependent fields. The significance of these transient fluctuations in surface wave drag will be discussed later in light of the results which follow.

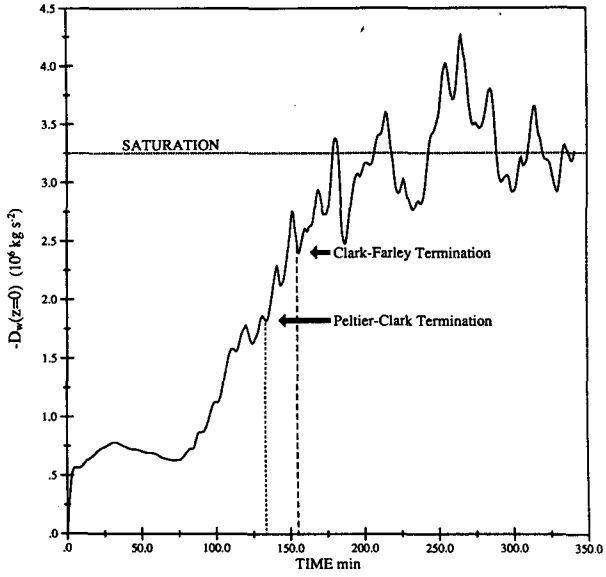

FIG. 6. Surface wave drag history for the 11 January 1972 windstorm simulation. Labeled on the diagram are those times at which Peltier and Clark (1979) and Clark and Farley (1984) terminated similar integrations. In this temporally extended integration the onset of surface wave drag saturation is observed and occurs after approximately 200 min of model time.

The total horizontal velocity at 150 min and 342 min of elapsed time in this simulation is displayed in Fig. 7 for a windowed portion of the model domain. For comparative purposes Figs. 7a and 7b are provided in contour format alongside grey scale renderings displayed at identical model times in Figs. 7c and 7d. In the analyses and discussions which follow, we have found the grey scale representations of the horizontal velocity field to be very stimulating of insight since they allow the detailed structure of the flow to be visualized with greater ease. Since it is this spatial structure that will be of primary interest to us rather than the numerical value of the field at any specific grid point, we will subsequently employ the grey scale rather than the contour format presentations of the horizontal velocity field in all that follows.

The model time of 150 min for which data are displayed in Fig. 7c (7a) approximately corresponds to the termination point of all previous simulations (PC79; DK83; CF84; D86) of this storm. Visible on the lee slope of the topography at this time is a region of strongly accelerated horizontal flow which extends to an elevation near 5 km. At this point in time the breaking region is located directly above this high velocity fluid through a range of elevations extending from 6–11 km. It is in this region that the wave mean flow interaction is focused which results in the deposition of counter flow momentum (Laprise and Peltier

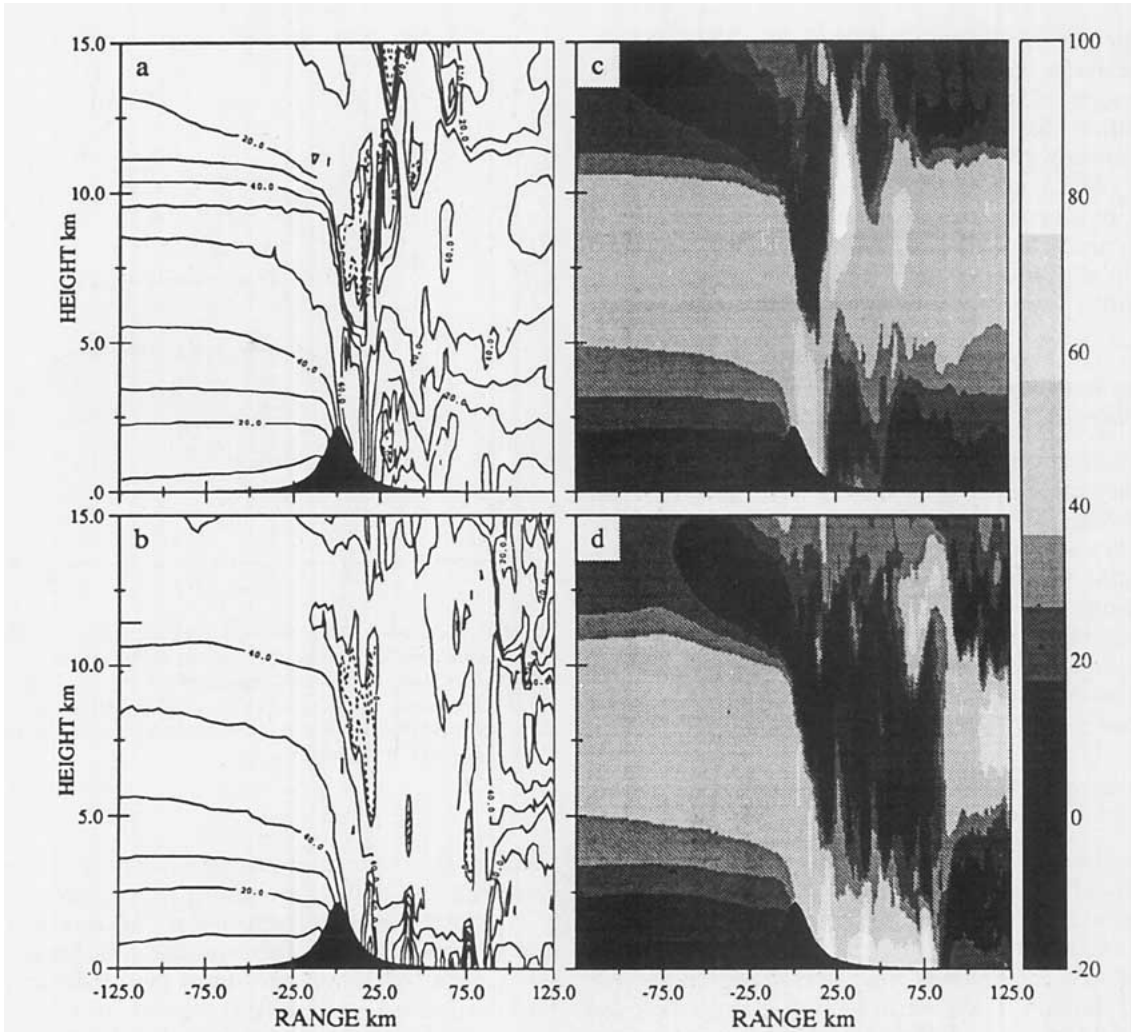

FIG. 7. Total horizontal velocity field for the simulation of the 11 January 1972 windstorm at (*a* and *c*) 150 min and (*b* and *d*) 342 min of model time. Note that at the latter time patches of high velocity surface wind occur at ranges of 15, 40, and 75 km to the lee of the topographic maximum.

1989a; 1989b). Consequently, the flow is strongly decelerated and a deep tongue of near stagnant fluid develops. This characteristic downslope windstorm configuration is now well understood and documented in the work cited previously.

The horizontal velocity field at the later time, Fig. 7d (7b), corresponds to a time by which the flow is well into the saturated regime of the surface wave drag history and reveals interesting new features of the mature downslope windstorm. The Chinook front here appears to have moved approximately 80 km downstream, leaving in its wake a jet of high velocity fluid which extends vertically from the ground to approximately the height of the topography. Over the same horizontal range, in the vertical cavity extending from 3–12 km elevation, a thick layer of slow and even reversed horizontal flow appears. Clearly though, the horizontal velocity in both these regions is highly inhomogeneous.

The strong low-level jet exhibits several localized regions in which high velocities in excess of 80 m s^{-1} appear at ranges of 15, 40, and 75 km downstream of the topography. These patches extend from the surface vertically to a height of 1–2 km. In the deep stagnant region above, localized patches of reversed flow are also present and appear directly above the high velocity pulses at the surface with approximately the same horizontal extent. The origin of these irregularities can be traced back to the upstream edge of the breaking region directly above the topographic maximum. Along this side of the stagnant tongue of fluid which outlines the breaking region, two elevated less intense patches of high horizontal velocity appear. Fluctuations of this nature were not present along the edge of the breaking region in the horizontal velocity plot at 150 min. It appears then that only after the downslope windstorm has sufficiently matured does strong transience in horizontal velocity develop.

The detailed temporal behavior of the horizontal velocity field will be discerned more clearly from the Hovmöller diagram of Fig. 8. This diagram provides a time history of surface wind speed for the same horizontal range as that displayed in Fig. 7. Before 100 min there is evidence of the strong lee wave signal discussed in section 2. Two regions of increased horizontal velocity appear at approximately 20 and 50 km downstream. In time, these regions approach vertical orientation indicating the zero phase speed of the lee wave resonance.

The breaking event at 75 min, however, causes a complete transformation of the flow and the steady state lee wave resonance is never reestablished thereafter. The strong effects of wave breaking are evident from the time of formation of the Chinook front at approximately 90 min and the steady increase in surface wind speed on the lee slope of the topography. The front remains nearly stationary at roughly 20 km downstream until approximately 175 min of integration. Subsequent to this time, it begins to move downstream with a mean speed of 5 m s^{-1}. It is important to note, as indicated on Fig. 8, that the Clark and Farley (1984) simulations were terminated after about 155 min of simulated time, just prior to the onset of downstream propagation of the front.

The strongest modifications of the flow occur in the region between the lee slope of the topography and the Chinook front. In this region, prior to the onset of downstream motion of the front, only a slight transience is visible in the strengthening horizontal wind. After the front begins to move, however, this region is marked by strong pulses of horizontal velocity that propagate the full length of the cavity. This regime of strong pulsation is clearly beyond the temporal range of the integrations performed in Clark and Farley (1984). In this regime each pulse appears on the lee slope, propagates with near uniform velocity downstream and abruptly stops at the Chinook front. The pulses have phase speeds that range from 18 m s^{-1} to 43 m s^{-1}. Looking back to Fig. 6 in which the surface wave drag history was presented, it is evident that the time at which the surface wave drag saturates is nearly coincident with the time at which the front begins to move and the time at which strong pulses in horizontal wind speed begin to appear (approximately 175 min into the integration). It would appear then, that for the 11 January event, strong transience in the surface

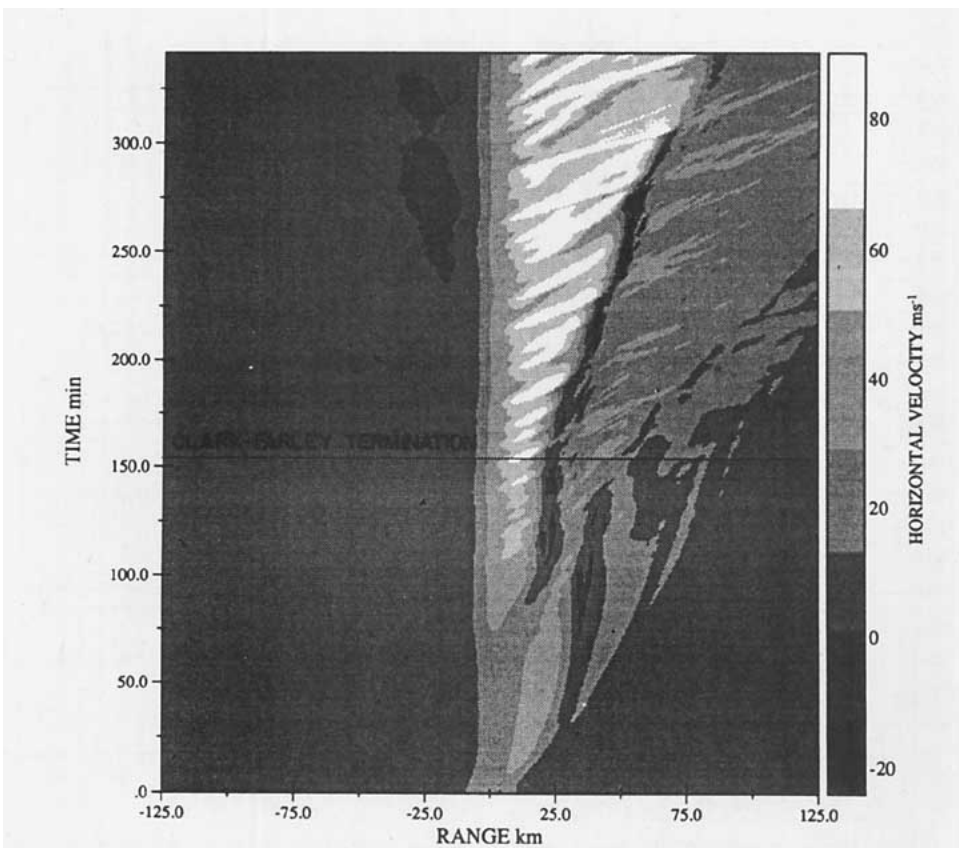

FIG. 8. Hovmöller plot of surface wind speed for the 11 January 1972 windstorm simulation. Labeled by the solid line on the diagram is the point at which similar calculations were terminated in a previous study of surface transience performed by Clark and Farley (1984).

wind speed develops simultaneously with the saturation of the drag curve (Fig. 6) and full maturation of the storm.

The Hovmöller plot also reveals that the expanded domain has resulted in very little upstream influence in the horizontal velocity at the surface with significant upstream blocking occurring only at very late times. Downstream of the Chinook front there appears a region of modestly enhanced wind speed that propagates downstream at a rate of approximately 13 m s^{-1}.

Five time series and corresponding power spectra for surface wind speed are shown in Fig. 9 at 10 km intervals downstream of the topography. These time series are to be compared to the observed time series of surface wind speed shown previously in Fig. 1. A high-pass frequency filter was convolved with each time series in order to remove low frequency structure associated with the passage of the front. Each filtered series is displayed in the form of deviations from the mean of the raw time series for ease of comparison.

The wind speed at the peak of the topography remains nearly constant in the simulation at 31 m s^{-1}. Further downstream at 10 km range, the average velocity has dramatically increased to approximately 60 m s^{-1} after the Chinook front has passed. At this range, fluctuations in the mean wind of 10–15 m s^{-1} magnitude begin to appear with periods of 8–20 min. As one looks to positions further downstream, the fluctuations become stronger and more localized. Before the front has passed the 20 km downstream position, there is an early increase in surface wind speed near 25–90 min. This is associated with the initial growth of the lee wave resonance discussed earlier. After the front has passed at roughly 175 min of model time, fluctuations in surface wind speed with an amplitude of 25 m s^{-1} appear—the strongest of which have periods of approximately 13, 14 and 17 min (see power spectrum). At 30 km and 40 km to the lee of the mountain, the fluctuations appear as sharp spikes that achieve peak wind speeds near 120 m s^{-1}.

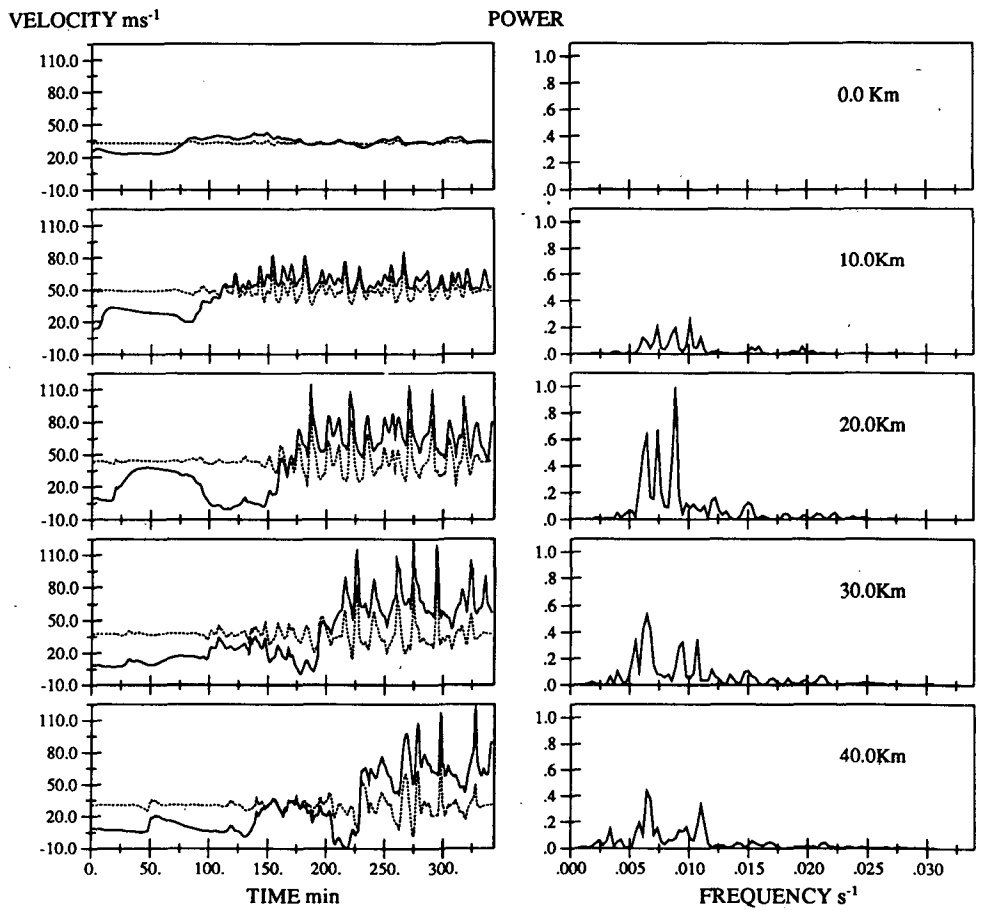

FIG. 9. Time series and associated power spectra of surface wind for the 11 January 1972 windstorm at 10 km intervals to the lee of the topography. Filtered time series (dotted) are displayed as deviations from the mean of the raw time series. These time series reveal that the simulation produces an O(10 min) quasi-periodic transience in surface wind which is consistent with that which was observed during the actual storm (Fig. 1).

A comparison of these time series with the anemometer trace in Fig. 1 reveals striking similarities with the strong lower frequency structure. The frequency of the pulses 10–30 km to the lee, fail within the band of 5–15 min period observed in Fig. 1. The nature of the the pulses 10–30 km to the lee, fall within the band of Neiman et al. (1988) that these pulses "maintain their identity in range and time." A comparison of the Hovmöller plot previously displayed in Fig. 8 with the equivalent "range–time" plots of Neiman et al. (1988, Figs. 13 and 18) clearly displays the similarity of the two phenomena, even though they derive from completely different events. This reexamination of the 11 January 1972 windstorm clearly indicates that the two dimensional model is itself fully sufficient to embody the phenomenon of strong surface transience that is such a pronounced characteristic of the observational data.

It should now be evident that the fluctuations found earlier in the surface wave drag history result from the strong pulses in surface wind speed. When a pulse appears on the lee slope of the topography we expect a sharp rise in surface wave drag. As the pulse propagates downstream, moving off the topographic maximum, the drag locally decreases. The complicated structure of these fluctuations in surface wave drag appear to result from a combination of the strength, periodicity and phase speed of the pulses. It is of interest to note that a different two-dimensional nonhydrostatic nonlinear numerical model employed in DK83 and D86 to perform the same calculation as that presented here, resulted in a perfectly smooth surface wave drag history (D86, Fig. 13). The steady smooth drag curve suggests little if any transience in the horizontal velocity at the surface. As a result, it is highly questionable whether this model can properly produce the pulsation phenomenon discovered here that fits so well the requirements of the observational data. Most probably the DK83 model formulation contains strong implicit numerical diffusion that retards the smaller scale physical process revealed by our relatively undamped model.

The presence of the strong pulses in a two-dimensional simulation of the 11 January 1972 windstorm, where they were not previously discovered, leads us to raise the question of the ability of even simpler incident flows to induce this same phenomenon. Constant wind and stability background profiles have often been exploited previously as the simplest flows in which downslope windstorms may be generated through wave breaking (e.g., Peltier and Clark 1983). As mentioned in section 1, during a downslope windstorm, these flows have also been previously expected to deliver uniform wind speeds at the surface in the lee of the topography.

b. *A downslope windstorm with upstream profiles of constant N and U*

The degree of supercriticality of a constant wind and stability flow is determined by the inverse Froude number $\mathrm{Fr} = hN/U$, where h is the height of the mountain. For the topographic shape employed here, specified by (10), it is well known (Miles and Huppert 1969) that supercritical flows are those for which $\mathrm{Fr} \geqslant 0.85$ that cause streamlines to overturn above the topography. Consequently, according to the theory of Peltier and Clark (1979), we should expect a downslope windstorm to occur in such circumstances. The greater the supercriticality the steeper the ascent to wave drag saturation.

For illustrative purposes a flow was selected with $U = 5$ m s^{-1}, $N = 0.01$ s^{-1}, $h = 500$ m and a mountain half-width $a = 5$ km resulting is a supercritical value of $\mathrm{Fr} = 1$. The same large domain was employed as in the previous section with length scales of $144 \cdot \Delta z = 18$ km in height and $722 \cdot \Delta x = 180.5$ km in width. With a hydrostatic wavelength of $\lambda_z = 2\pi U/N = \pi$ km, the upper absorber was maintained over 45 grid points giving a depth for this region of almost $2\lambda_z$. Following the work of Laprise and Peltier (1989a) in which similar integrations were performed on a slightly coarser grid, the eddy mixing parameterization scheme was turned off for this calculation by setting $k = 0$ in (4). A time step of $\Delta t = 5$ sec was implemented for the 12.5 h of simulated real time.

The surface wave drag history for this integration is displayed in Fig. 10. The general appearance of the drag curve is quite different from that found for the more meteorologically realistic 11 January calculation. The breaking event appears to begin immediately after startup as evidenced by the early and continual rise of the surface wave drag. The growth of the drag continues for a very long time occupying the first three-fourths

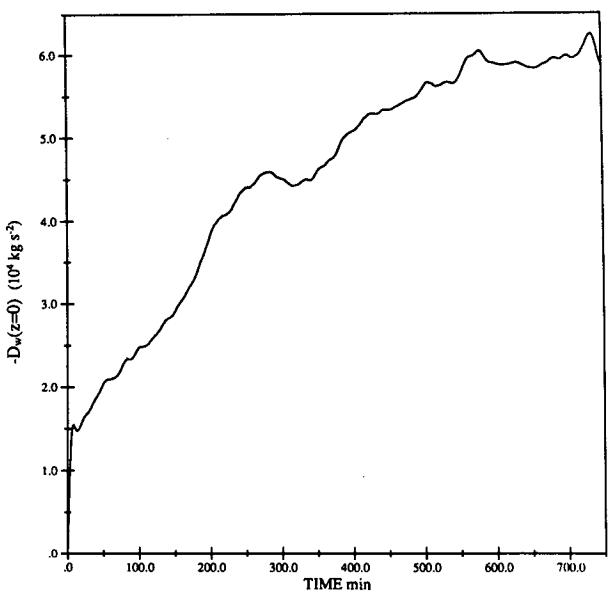

FIG. 10. Surface wave drag history for a constant N and U incident flow with $U = 5$ m s^{-1}, and $N = 0.01$ s^{-1}, $\mathrm{Fr} = 1$, $h = 500$ m and $a = 5$ km.

of the simulation. For the last 200 min of integration it appears to have saturated at a value of roughly 6.0 $\times 10^4$ kg s^{-2}. Fluctuations are present in the surface wave drag thereafter, but they appear as rather smooth small amplitude oscillations that do not seem to amplify with time.

In Figs. 11a–c the total horizontal velocity field is displayed after integration times of 400 min, 567 min and 750 min respectively for the lower right-hand portion of the model domain. At 400 min a strong surface jet of 10–15 m s^{-1} strength appears, ranging from the lee slope of the topography to approximately 35 km downstream. This lee jet again extends vertically from the ground to roughly the height of the topography. Directly above this jet is once more a region of decelerated flow of strength 0–2 m s^{-1} which extends vertically from 1 km to 3 km. Again, this near stagnant region is the result of wave–mean flow interaction in

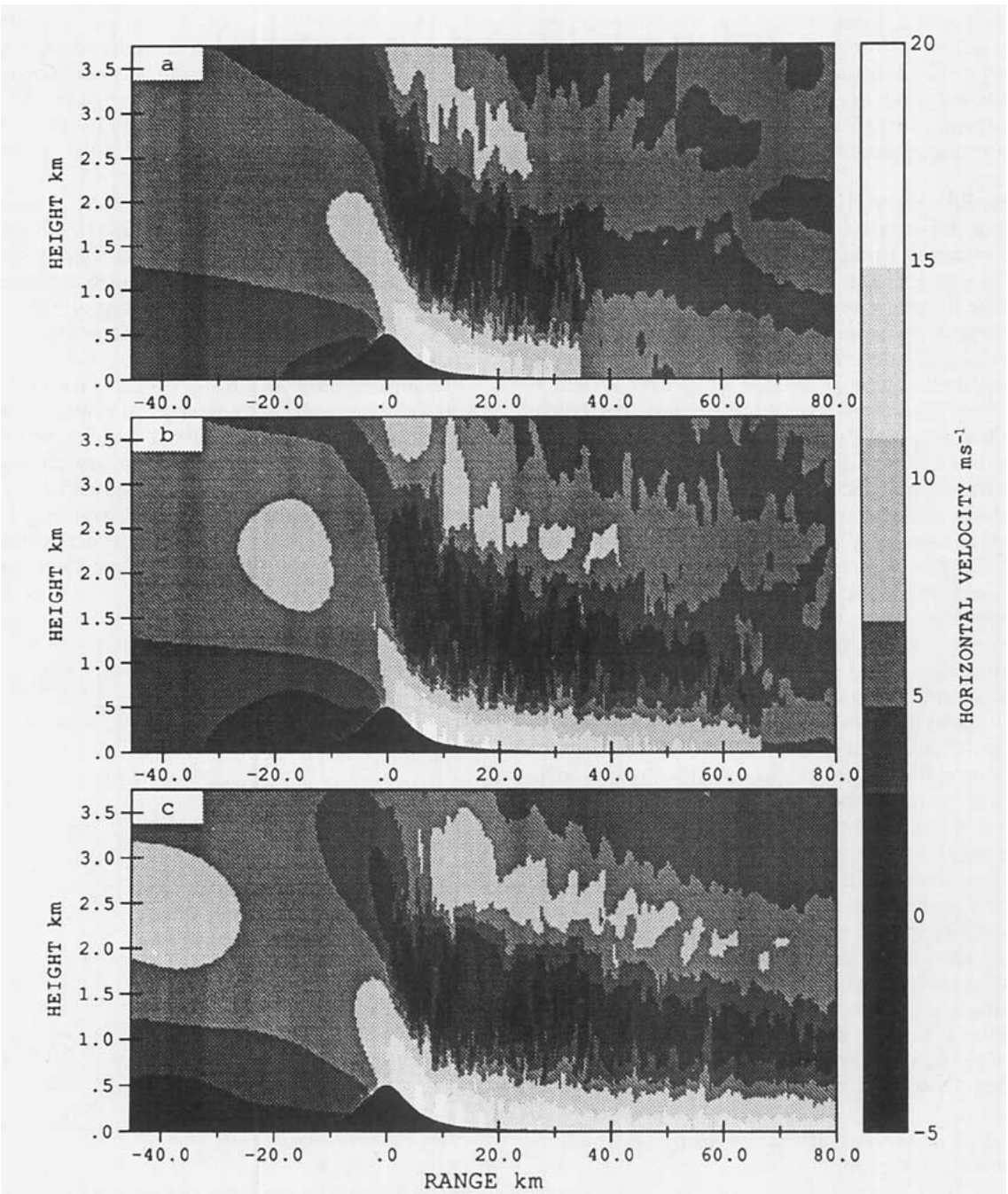

FIG. 11. Total horizontal velocity fields for the constant N and U case at (a) 400 min (b) 567 min and (c) 750 min of model time.

the breaking region approximately 2 km above the lee slope of the topography. These two regions are similar to those found previously in Fig. 7d (7b) for the 11 January event in the sense that they lack uniform intensity. Embedded within the strong surface jet, two narrow patches of high velocity fluid appear in which speeds from 15–20 m s^{-1} obtain at positions 7 and 16 km downstream. There are also narrow vertically oriented patches of near zero velocity fluid in the elevated decelerated zone directly above the high velocity regions in the low level jet.

At 567 min the surface jet and stagnant region extend nearly 70 km downstream. On the lee slope of the topography, several narrow closely spaced patches of high velocity fluid appear at this time, with speeds in excess of 15 m s^{-1}. These patches extend over a distance of 20 km downstream. By 750 min the Chinook front has moved completely out of the model domain. On the lee slope, between 5–20 km range, we now see four very well defined patches of high velocity fluid. Directly above the two most intense of these pulses lie regions of decelerated fluid at a height of approximately 1.5 km. The structure of these anomalies in the total horizontal velocity appears very similar to those found for the 11 January windstorm calculation discussed previously.

Beyond the surface transience discovered in the horizontal velocity field are several other interesting features. It is important to note that at 750 min, after the Chinook front has moved completely out of the model domain, no evidence of horizontal velocity field contamination appears at the outflow boundary. This clearly demonstrates the efficiency with which the open downstream boundary condition advects disturbances out of the model domain.

There is also an interesting transience in the horizontal velocity field upstream of the topography. At 400 min of model time on the windward side of the mountain, a region of strong blocking appears where the flow has been reduced to 1–2 m s^{-1} strength. Directly above is a region of fluid from 1–2 km altitude with a velocity of 7–10 m s^{-1} that is part of a plume stemming from the fast moving jet in the lee of the topography. At 567 min a bubble of blocked fluid, 0.75 km deep, has developed 20 km upstream. Directly overhead, centered at an elevation of 2.25 km, appears an elliptical region of fast flow. The high velocity plume at this time has receded back to a position directly over the topographic maximum. By 750 min both regions have expanded horizontally and appear to have propagated in unison upstream a distance of 40 km. At this time there is very little blocking on the windward slope of the topography. Also, the plume of high velocity flow stemming from the lee surface jet has begun to inflate again by bending upstream, suggesting the production of another pulse. It appears then that there is also some transient phenomenon occurring upstream that may be of a wholly different nature from that discovered in the lee of the topography.

A detailed study of the upstream effects associated with downslope windstorms, generated with constant N and U incident profiles, was previously conducted by Pierrehumbert and Wyman (1985, hereafter PW85). A hydrostatic numerical model with a Gaussian topographic profile was employed in their investigation. For the simple nonrotating case presented here, they determined that after a sufficient time a steady rather than transient blocking would be produced upstream of the topography. There is evidence in PW85 (Fig. 7), however, of a transience in the upstream blocking with a nature similar to that found here. As a result of the hydrostatic approximation employed in PW85, the propagation of the double lobed structure of high over low velocity distorts progressively as it propagates upstream. The result is a smoother more steady blocking than that found in the calculation presented here.

A Hovmöller diagram of surface wind speed is presented in Fig. 12 for the full horizontal range of the domain. In the first 100 min two regions of decelerated flow of strength 3–4 m s^{-1} have expanded from the topography outwards, reaching the upstream absorber and downstream outflow boundary. Between these two regions, on the lee slope of the topography, the mean wind increases, resulting in speeds of 6–10 m s^{-1}. The Chinook front appears to form just after 100 min and moves very slowly downstream for the next 100 min. From 200–300 min the Chinook front accelerates to a speed of 3 m s^{-1}, which thereafter remains very steady. At 625 min the Chinook front moves out of the model domain. As the front accelerates, strong pulses of surface wind are generated with speeds in excess of 15 m s^{-1}. Unlike the 11 January windstorm calculations, all the pulses produced in this case appear to propagate downstream with the same phase speed. A uniform speed of 7 m s^{-1} and a horizontal wavelength of $\lambda_x \approx 3$ km is found to be characteristic of all of the pulses. Whereas the corresponding pulses generated in the simulation of the 11 January storm at Boulder, Colorado propagated the full distance between the lee slope of the topography and the Chinook front, those that develop in the constant N and U calculation decay well before they reach the front. Nevertheless, there is evidence from the Hovmöller plot at 300 min that, as in the 11 January case, the pulses cannot propagate further than the front itself.

In the 11 January windstorm calculation, the saturation of the surface wave drag appeared to coincide with the onset of downstream motion of the front and with the onset of the production of strong pulses in the horizontal velocity. The results from the constant N and U calculation further clarify the nature of the relationship between these three events. From the Hovmöller plot for this case, it is apparent that a strong production of pulses occurs only during the episodes from 200–325 min and 500–750 min of model time. From the surface wave drag history previously presented in Fig. 10, we see that these two time intervals

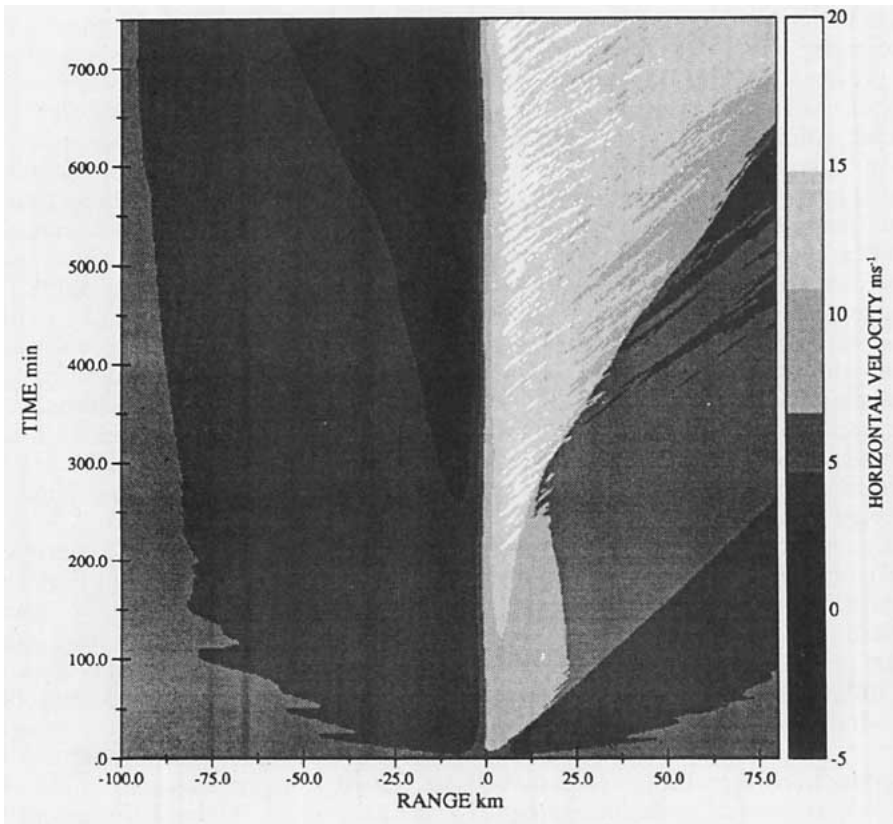

FIG. 12. Hovmöller plot of surface wind speed for the constant N and U case.

roughly coincide with the occurrence of local wave drag saturation. It appears, therefore, that the wave drag must be saturated for the efficient production of the pulses. Once the drag curve locally saturates, the front begins to accelerate downstream. Further growth in wave drag causes a slight deceleration of the downstream motion of the front.

Strong upstream blocking is clearly evident in Fig. 12. Following 250 min of model time a region of slow 1–3 m s^{-1} flow develops on the windward slope of the mountain and begins to propagate upstream. At 500 min a region of 0–1 m s^{-1} fluid appears on the upstream slope but dissipates after 100 min. This is associated with the bubble of slow, blocked flow that propagates upstream which was described earlier. The initial blocking that reaches the upstream absorber at 100 min only penetrates three-fourths of the way into the sponge for the next 650 min of integration. In this time no reflections at the inflow boundary appear.

Five time series and power spectra of surface wind speed are presented in Fig. 13 at 5-km intervals downstream from the topographic maximum. These are prepared and displayed in the same manner as were those for the previously discussed 11 January case. Inspection of these time series for increasing downstream range demonstrate that strong transience in surface wind speed develops immediately after the Chinook front has passed. At 10 km range, peak winds of 17 m s^{-1} are obtained and a strong 10.5 min period is prevalent in the power spectrum. At 15 km downstream, the fluctuations in surface wind velocity reach maximum amplitude with peak speeds of 19 m s^{-1}. These fluctuations extend over periods ranging from 5–20 min. There is a significant power loss at greater distances due to the decay of these pulses noted on the previously described Hovmöller plot. These time series make obvious the fact that a constant wind is not obtained in the lee surface jet of a downslope windstorm generated from uniform N and U incident flows in two spatial dimensions.

This investigation clearly establishes that the physical processes responsible for the pulses of surface wind are not suppressed when the breaking event is initialized with idealized incident profiles of constant wind and stability. Therefore, the occurrence of the pulsation phenomenon appears insensitive to the upstream conditions that precipitate the downslope windstorm. In the next subsection we initiate a simulation of the 11 January 1972 event, employing slight modifications to the observed upstream profiles of temperature and horizontal wind so that a comparison may be made with the results of section 3a and an assessment made of the sensitivity of the details of the pulsation to relatively minor variations of the forcing.

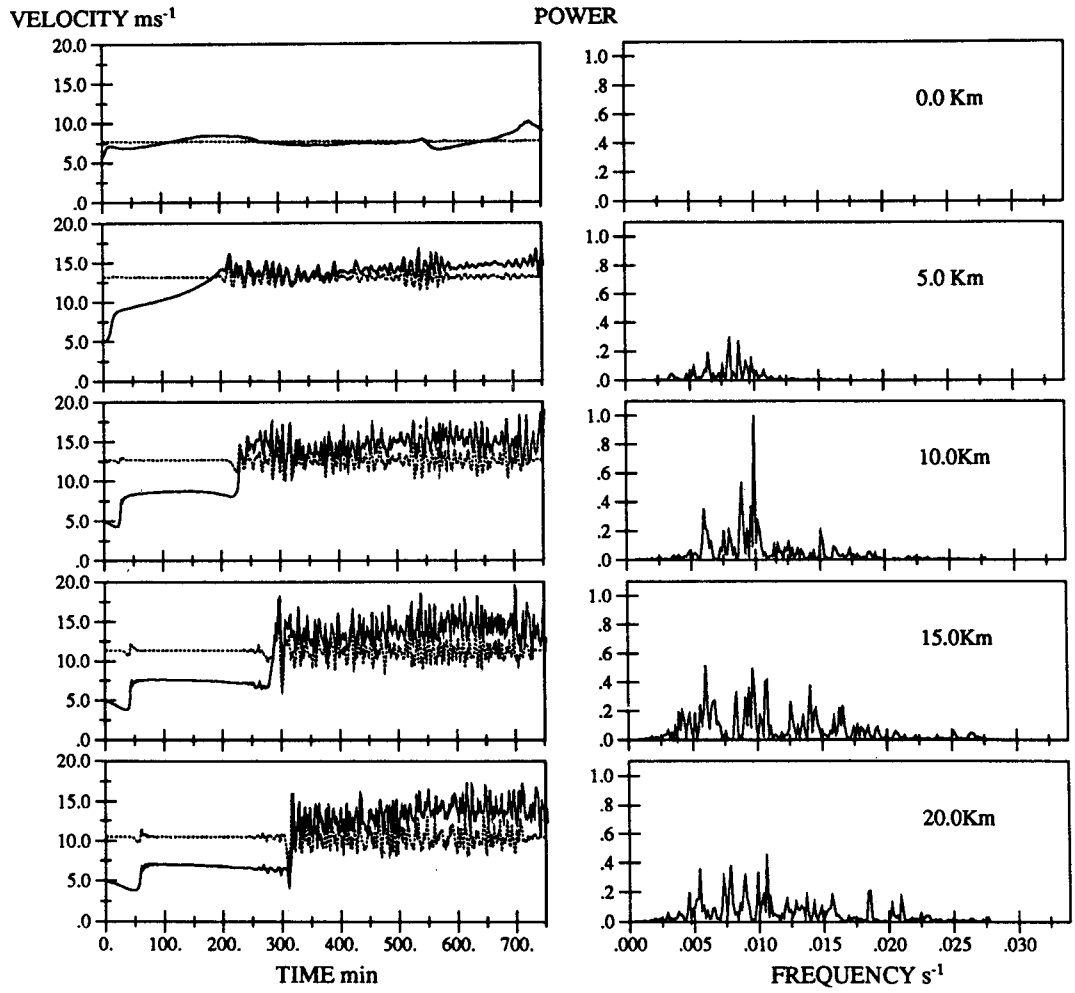

FIG. 13. Time series and associated power spectra of surface wind at 5 km increments downstream of the topography for the constant N and U case. Filtered series (dotted) are displayed as deviations about the mean of the raw time series.

c. Windstorm development in a modified 11 January 1972 mean state

Because of the intensity of the surface wind pulsations predicted to be characteristic of the 11 January storm, in this subsection we will consider slight variations of the observed upstream profiles in an attempt to determine how strongly these pulses of surface wind are tied to the details of these profiles. Figure 14 displays the 11 January profiles (solid curves) overlain by those employed for the calculation to be discussed in this section (dotted curves). In the new profiles, the temperature at all levels is greater by approximately 15°–20°C and the stable layer (inversion) near 3 km elevation is deeper and closer to the surface. The horizontal velocity profile appears smoother and is altered only slightly. The integration was performed on the same domain as was the 11 January calculation discussed previously and was initiated with a time step of $\Delta t = 4$ s, which was reduced to $\Delta t = 3$ s as the flow developed. After 200 min of model time the integration was restarted every $15\Delta t$ rather than $20\Delta t$ to obtain frequent history saves (due to model formulation).

In Fig. 15 the surface wave drag history for the 342 min of model integration is presented. The drag prior to breaking is roughly 1.0×10^6 kg s^{-2} and is somewhat higher than the value of 6.0×10^5 kg s^{-2} found previously in Fig. 5 for the 11 January case. The breaking event again occurs after approximately 75 min of integration and the wave drag saturates near 150 min of model time after having achieved a magnitude of roughtly 3.4×10^6 kg s^{-2}. Even though the level of saturation is very close in both calculations, there is only a 3.5-fold increase in wave drag in this case compared to the sixfold growth reported for the 11 January storm. The fluctuations in the wave drag history appear to achieve smaller amplitude and are more evenly modulated about the level of saturation as opposed to

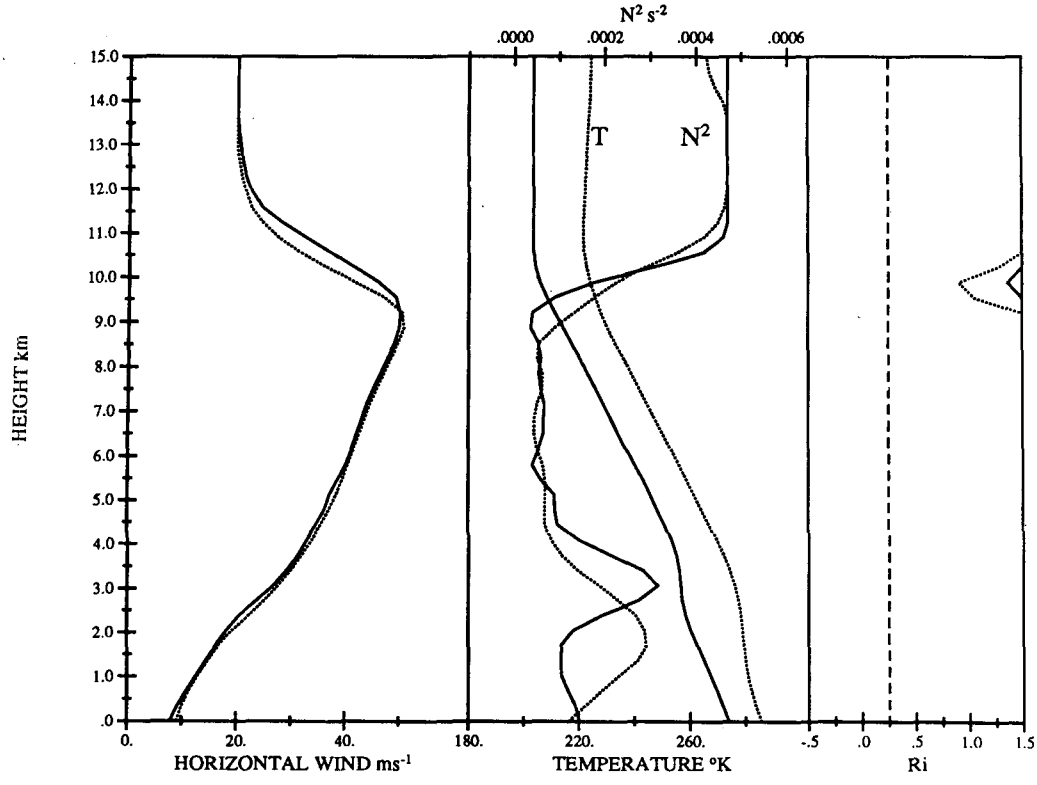

FIG. 14. 11 January 1972 (solid) and modified 11 January 1972 (dotted) upstream incident profiles.

the more radical departures found for the 11 January case in Fig. 6.

A Hovmöller plot of surface wind speed is provided in Fig. 16 for a windowed portion of the model domain for this modified case. The Chinook front forms after 75 min of model time and is stationary until approximately 150 min. At this time, it begins to move downstream with a constant speed of 6.4 m s^{-1}. The motion of the front is very smooth in the modified case compared with that found earlier in Fig. 8 for the 11 January event. There is some evidence of small amplitude pulses on the lee slope of the topography while the front is stationary. After the front begins to move, strong pulses are generated and propagate from the lee slope to the Chinook front. As in the constant N and U case, all the pulses travel downstream with the same uniform phase speed, which in this case is of magnitude 22.5 m s^{-1}. The pulses occur with a greater regularity than those found in the 11 January simulation. A wavelength for the spatial separation of the pulses, measured from Fig. 16, gives an estimate of $\lambda_x \approx 16$ km.

A slightly stronger upstream blocking appears in the modified storm. After the surface wave drag saturates at 150 min, a region of blocked flow appears approximately 25 km upstream of the topography. This region moves upstream but halts near 60 km at 250 min and proceeds no farther until the end of the simulation. A region of smaller scale disturbances propagates downstream ahead of the Chinook front with a greater speed of 9 m s^{-1}.

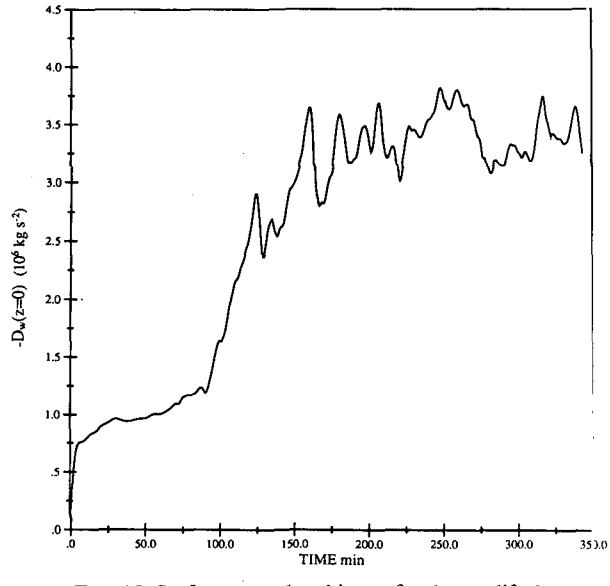

FIG. 15. Surface wave drag history for the modified 11 January 1972 case.

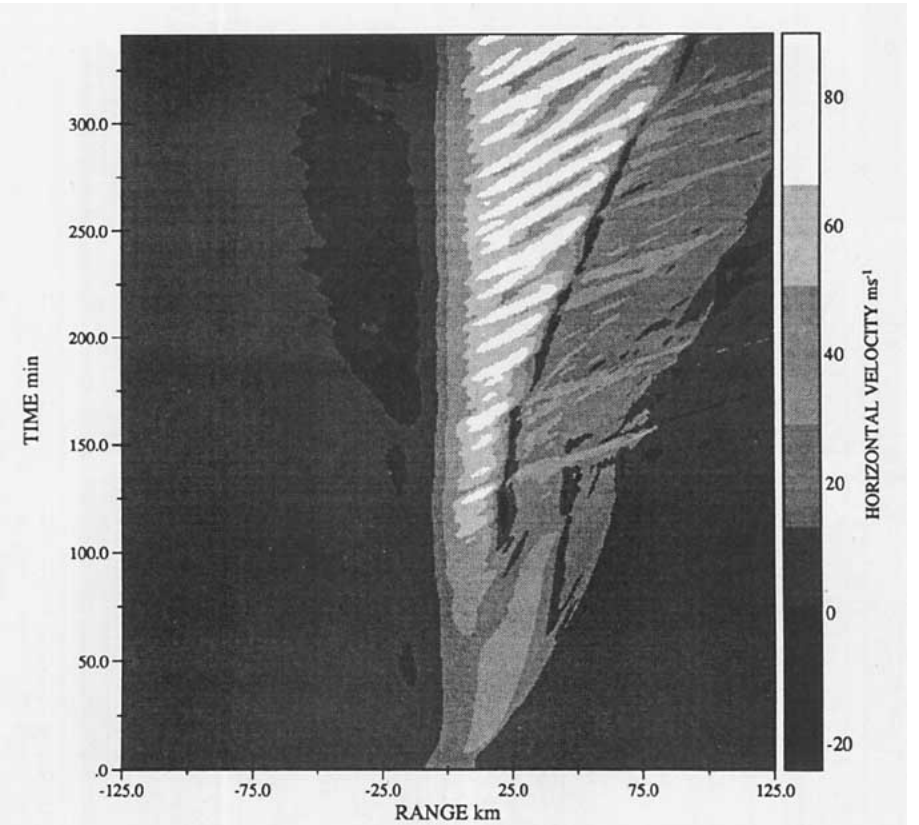

FIG. 16. Hovmöller plot of surface wind speed for the modified 11 January 1972 case. Note how the pulses occur with a greater spatial and temporal periodicity than those observed in the Hovmöller plot displayed earlier for the 11 January Boulder windstorm simulation (Fig. 8).

Six plots of total horizontal velocity are presented in Fig. 17. The 6 panels, (a)–(f), span a model integration time of 200–215 min. This closely spaced succession of samples reveals the process by which a high velocity pulse appears at the surface. Initially, at 200 min (Fig. 17a), four patches of high velocity fluid with maximum speeds between 60–100 m s^{-1} are present in the range from 5 km upstream, at an elevation of 7.5 km, to 25 km downstream at the surface. Associated with each of these, directly overhead, is a region of reversed flow embedded in the tongue of stagnant fluid aloft. If we follow the evolution of the moderate 60 m s^{-1} pulse directly above the topographic maximum at 200 min, we see it descend to the surface at 203 min and by 206 min overtake the next pulse 10 km further downstream. At 209 min, in their place appears one strong >80 m s^{-1} pulse which can be found in the Hovmöller plot of Fig. 16. By 212 min (Fig. 17e), the process comes full circle and the state of the pulses appears almost identical to that found at 200 min. During this 12 min interval, a new disturbance has been generated high above the topography that replaces the particular pulse described above. It appears from this sequence that the strong surface pulses found in the Hovmöller plot of Fig. 16, are originally generated roughly 9 km aloft on the leading edge of the breaking region slightly upstream of the mountain peak. From there, they grow in strength and depth as they move downstream, eventually reaching the surface.

Figure 18 presents the horizontal velocity field after 275 min of integration. From this plot the deep vertical structure of four surface pulses can be discerned in great detail. The pulses of high velocity wind appear to reach maximum intensity at the surface and extend vertically through a depth of nearly 2 km. Each associated overlying patch of fluid in which the flow is reversed appears vertically oriented from 4–9 km. Above this height these patches tend to tilt or are kinked in the downstream direction.

Time series and power spectra of surface wind speed are displayed in Fig. 19 at downstream positions equivalent to those previously presented for the 11 January storm in Fig. 9. Close to the mountain, the time series appear very similar. At 20 km downstream, however, there are significant differences. In the 11 January simulation, at this range, the amplitude of the fluctuations varied greatly and three sharp frequencies were present in the power spectra. The modified calculation produces fluctuations that are very nearly the

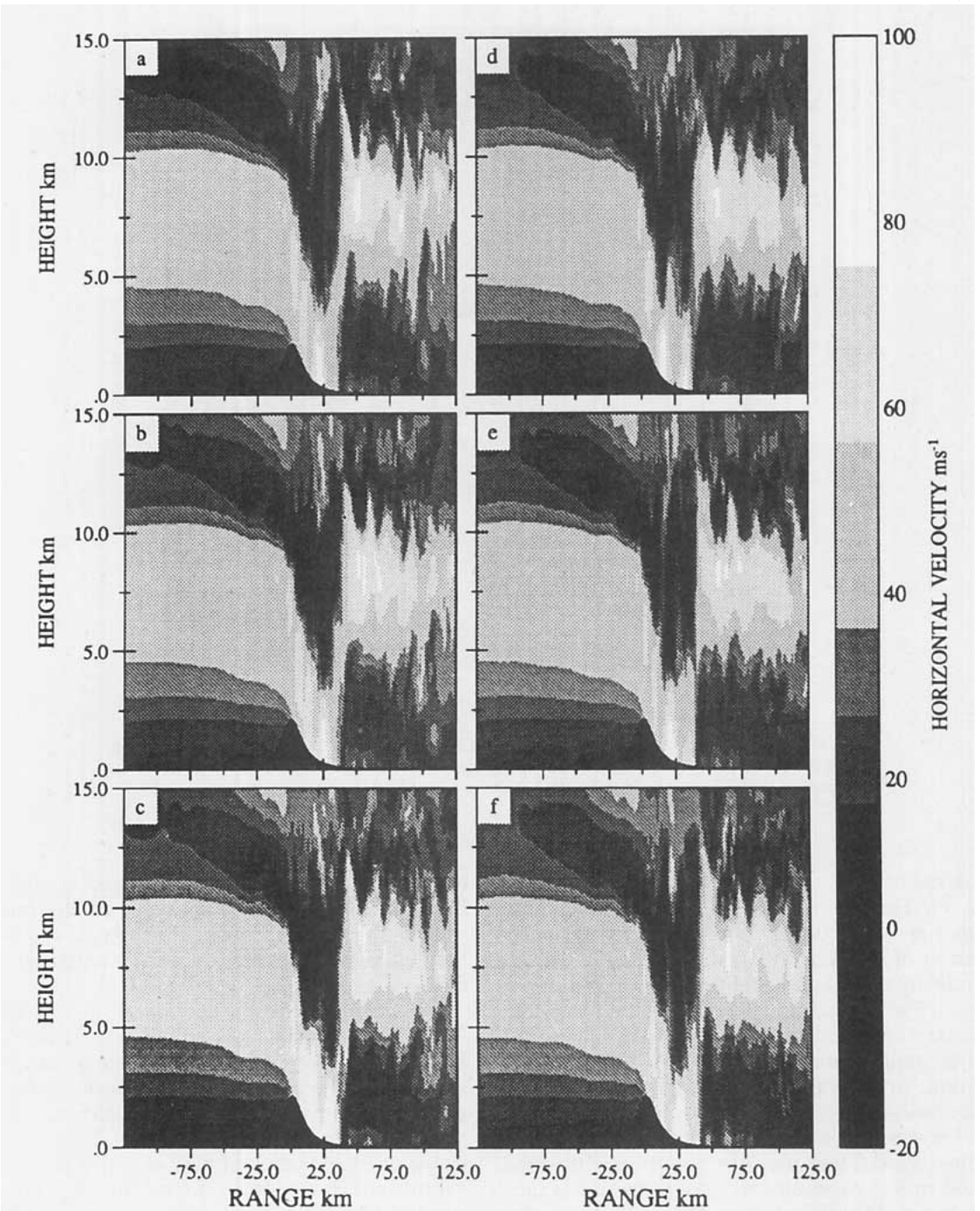

FIG. 17. Total horizontal velocity fields for the modified 11 January 1972 case at (a) 200 min, (b) 203 min, (c) 206 min, (d) 209 min, (e) 212 min and (f) 215 min of model time. Note how the moderate pulse directly above the topographic maximum at 200 min may be traced in time as it makes its way down to the surface to become a strong pulse by 209 min.

same amplitude with the spectra being characterized by the presence of one pronounced period that is close to 12 min. The same is found further downstream at 30 km range. Unlike the 11 January case, the fluctuations do not evolve into sharp spikes as they propagate downstream. From 10 km to greater than 30 km downstream, the modified flow creates a lee surface jet dominated by uniform amplitude fluctuations in surface wind speed with one well-defined frequency. It can be seen then, that a slight modification in the up-

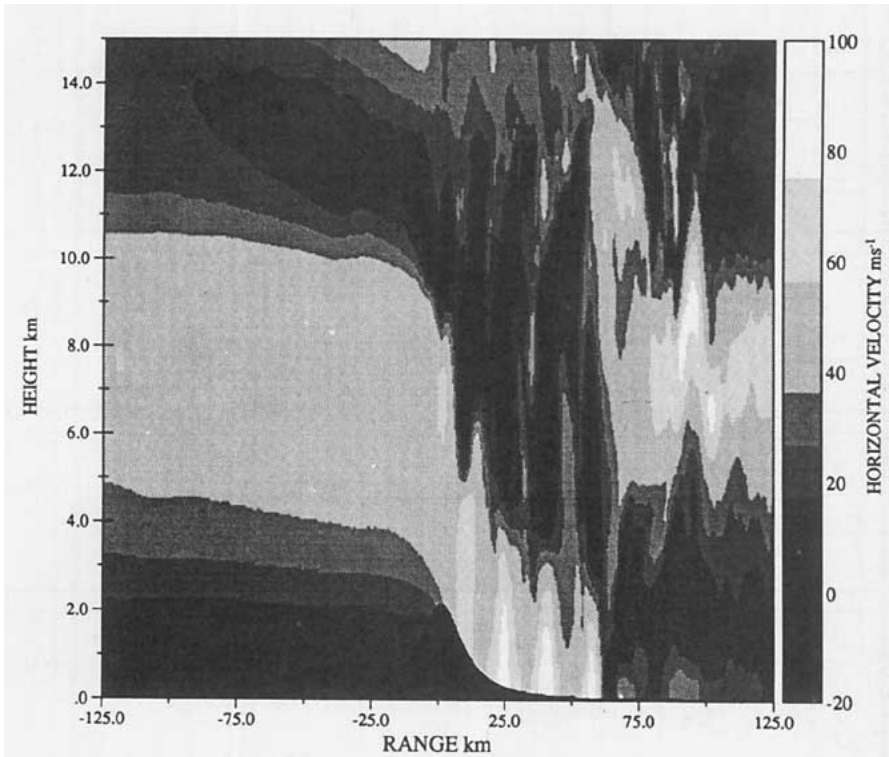

FIG. 18. Total horizontal velocity field for the modified 11 January 1972 case at 275 min.

stream profiles has served to enhance the regularity of the pulses in both space and time.

d. *Effects of supercriticality on the modified 11 January 1972 storm*

A series of calculations was initiated to investigate a further influence on the transient characteristics of the modified 11 January, Boulder, Colorado flow—that associated with the degree of supercriticality. This study was conducted by fixing the upstream profiles of wind and temperature and varying only the height of the mountain. From the analysis of this upstream flow presented in the previous subsection, we know that a mountain height of $h = H_J$ ($H_J = 2.044$ km) produces a supercritical flow resulting in a downslope windstorm and dramatic rise in surface wave drag. The wave drag history for this case is reproduced in Fig. 20 along with those generated for 7 additional flows employing topographic heights in the range $0.5H_J \leqslant h \leqslant 1.07H_J$.

The integration employing a mountain height of $h = 0.5H_J$ results in a drag history that stays level after startup with a magnitude of 3×10^5 kg s^{-2}. As the mountain height is increased, wave breaking begins to occur but cannot be sustained for mountains that have heights ranging up to $0.891H_J$. When the height of the topography is increased slightly beyond this value to $h = 0.906H_J$, the drag grows continuously from 80 min of model time to the termination of the integration at 200 min. Thus, two integrations employing topography that differs only by 1.5% elevation give rise to two flows that differ dramatically in the limit of long time. It seems then that the two regimes of subcritical and supercritical flow are separated by a very sharp threshold in accord with the analysis of the stability of such nonlinear waves recently presented in Laprise and Peltier (1989a).

A long integration with $h = 0.935H_J$ is also presented in Fig. 20. The breaking event begins at 80 min and the slow steady growth of the wave drag continues until roughly 250 min. This calculation, employing a mountain height only 6.5% lower than that used in the modified 11 January case, took a full 100 min longer to reach wave drag saturation. For $h = 1.07H_J$ the breaking event appears earlier at roughly 65 min. Thereafter the drag increases very rapidly and saturates after 100 min of model time.

An important feature of these wave drag histories is the level at which wave drag saturation occurs for simulations in which a downslope windstorm was produced. For the integrations with $h = 0.935H_J$, $1.0H_J$ and $1.07H_J$, implying ascending degrees of supercriticality, the wave drag saturates at roughly equivalent values near 3.0×10^6 kg s^{-2}. This suggests the important result that the level of wave drag saturation is independent of the degree of supercriticality of the flow. The various degrees of supercriticality seem to affect only the rate at which the drag grows to saturation after breaking begins. The greater the supercriticality, the

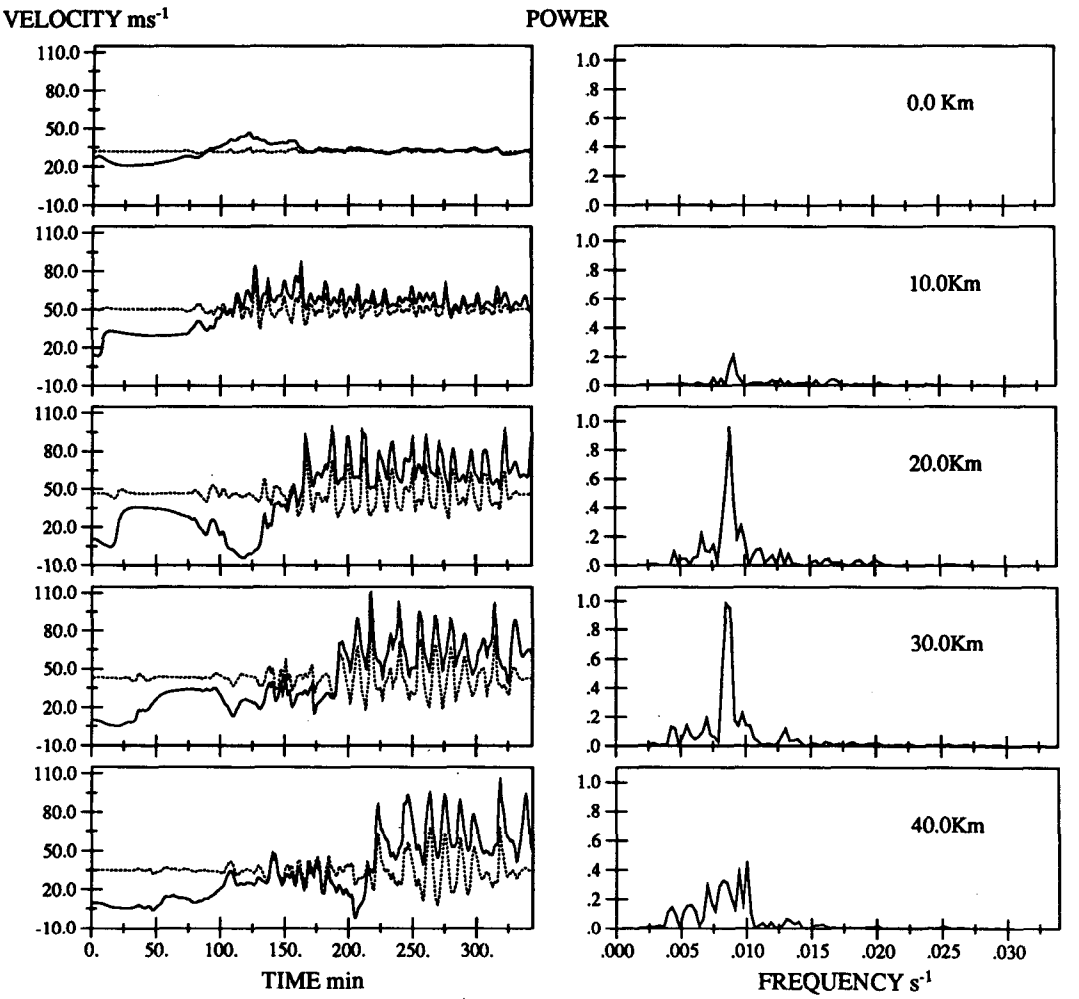

FIG. 19. Time series and associated power spectra of surface wind speed at 10 km increments downstream of the topography for the modified 11 January 1972 case. Filtered time series (dotted) are displayed as deviations about the mean of the raw time series.

more rapid the transition into the high drag state as initially suggested in Peltier and Clark (1979).

These calculations also allow us to investigate the relationship between the degree of supercriticality and the nature of the strong pulses of surface wind discovered earlier in this section. A Hovmöller plot of total horizontal velocity for the integration that employed a mountain height of $h = 0.935H_f$ is displayed in Fig. 21. It is presented for the same horizontal range as that exhibited previously in Fig. 16 for the modified 11 January case. In this simulation the Chinook front forms after 75–100 min of model time and remains stationary for the ensuing 150 min. During this time only small amplitude fluctuations of surface wind appear between the lee slope of the mountain and the front. At roughly 250 min the front accelerates to an average speed of 6.3 m s^{-1} matching the value found from Fig. 16 for the higher mountain. Appearance of the strong downstream pulses in horizontal wind speed again coincides with the onset of downstream movement of the front and, from Fig. 20, the saturation of the surface wave drag. The individual pulses propagate downstream with uniform phase speeds that range from 25.5 to 35.5 m s^{-1}. Very little blocking appears at the surface upstream of the topography for this lower mountain height. Downstream, ahead of the Chinook front, an envelope of smaller amplitude disturbances propagates with a speed of 13.5 m s^{-1}.

Earlier in this section it was found that the pulses were generated efficiently whenever the surface wave drag locally saturated and that the acceleration of the front coincided with this event. These ideas are further vindicated by the results of the criticality experiments presented above. By reducing the mountain height 6.5%, the point in time at which wave drag saturation occurred was delayed for 100 min. Rather than accel-

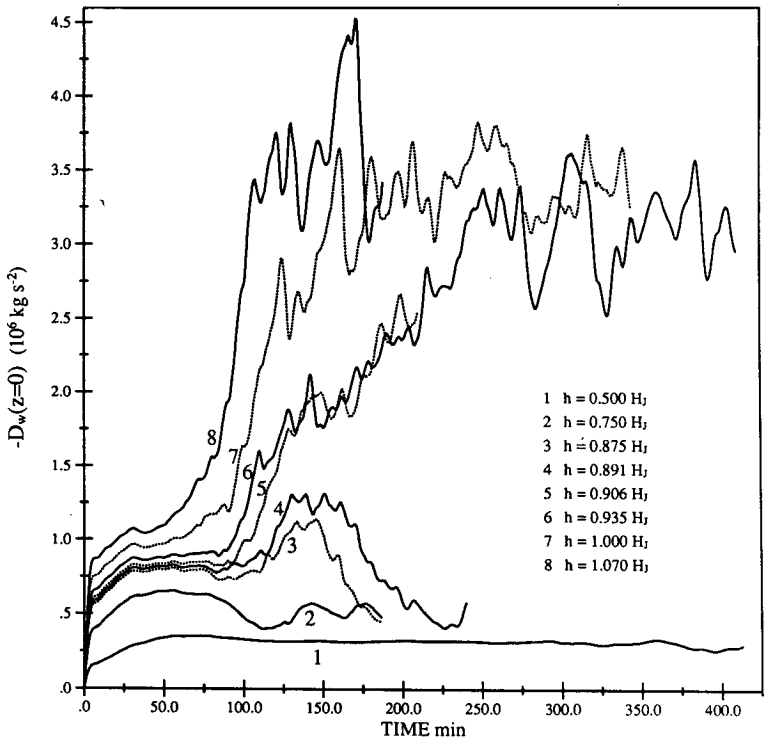

FIG. 20. Surface wave drag histories for supercriticality experiments employing the modified 11 January 1972 profiles. $H_J = 2044$ m is the height of topography employed previously for this background. Note how a difference of only 1.5% in the height of the topography results in two flows with dramatically different final drag states (curves 4 and 5).

erating from rest at 150 min, as in the modified 11 January case, the onset of the front's downstream motion also was delayed by 100 min. This provides even stronger evidence that the two events of wave drag saturation and frontal acceleration are closely connected.

The pulses of high velocity wind appear to be most strongly affected by the decrease in supercriticality. For the higher mountain they were very regular in time and space. When the mountain height was reduced, however, this regularity too appears to have been reduced. Presented in Fig. 22 are time series and power spectra of surface wind at various positions to the lee of the topography for the case employing a mountain with $h = 0.935 H_J$. At 10–15 km downstream fluctuations appear and two bands of periods are most prevalent in the ranges 10.5–14 min and 6–7 min. Further downstream, in the 20–25 km range, the fluctuations grow much stronger and the lower frequency band dominates with two periods of 10.5 min and 13 min. It appears then that the spectrum of pulses is less monochromatic than was found to be the case for the higher mountain. These results indicate that a significant modification of the spatial and temporal characteristics of the strong pulses of surface wind may be affected with only slight changes in the supercriticality of the flow.

e. Effects of $2\Delta x$ horizontal spatial filters on the pulsation phenomenon

All of the simulations presented thus far in this section have been performed with no horizontal spatial filtering applied to $2\Delta x$ waves. Given that the pulsation phenomenon discovered here was not previously found in similar numerical simulations that employed such in situ filtering, it would seem a reasonable concern that the pulses might be the result of numerical noise aliased up from smaller wavelengths rather than the result of a resolved physical process. In this subsection we address this question by presenting a simulation identical to that described in section 3c except that horizontal spatial filters designed to damp $2\Delta x$ structure were applied. A second order (∇^2) filter was employed in a region of the domain of width $45\Delta x$ interior to the inflow and outflow boundaries. Interior to these inflow and outflow columns a fourth order (∇^4) filter was employed in two bands of width $45\Delta x$. The remainder of the domain (bounded by $90\Delta x$ from the inflow and outflow boundaries) was smoothed by a sixth order (∇^6) filter. These filters were all designed to completely damp $2\Delta x$ waves in a time interval of $4\Delta t$.

The surface wave drag history from this simulation is presented in Fig. 23 (solid line) where it is overlain

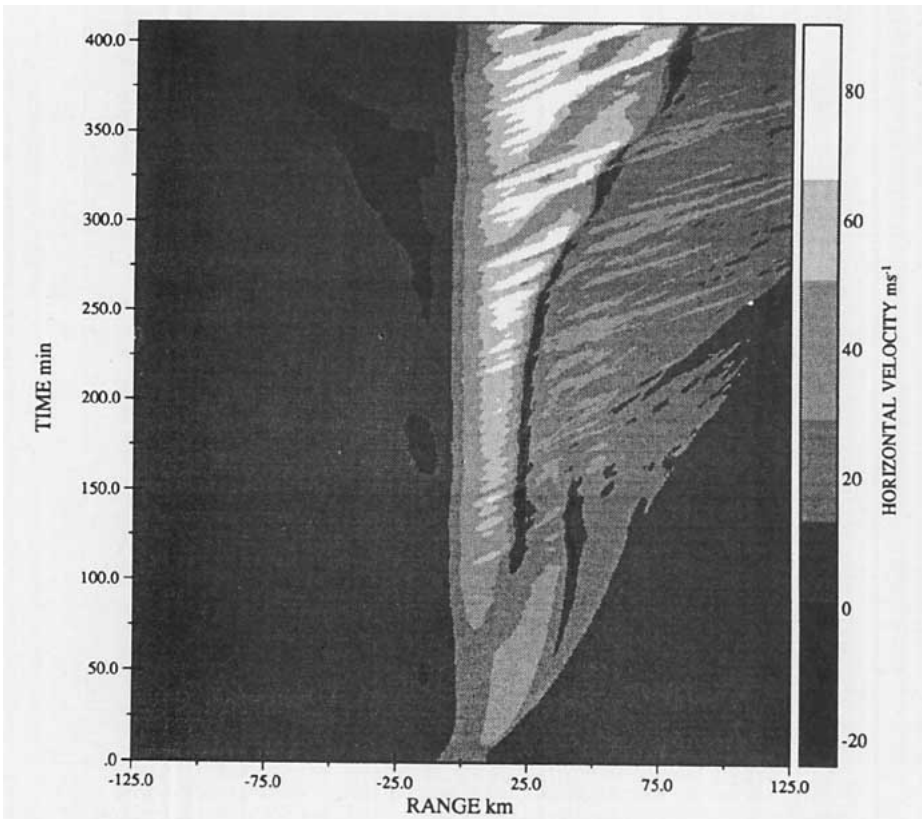

FIG. 21. Hovmöller plot of surface wind speed for the modified 11 January case with mountain height $0.935H_J$. Through the reduction in supercriticality, the initial downstream movement of the front has been delayed by 100 min. Note that the saturation of the surface wave drag (Fig. 20, curve 6) has also been delayed by an equivalent amount of time.

with the one obtained in section 3c and previously displayed in Fig. 15 (dotted line). Both surface wave drag histories display the same general behavior. Spatial filtering of $2\Delta x$ waves does not appear to alter the time at which wave breaking occurs, the rate at which the drag rises towards saturation or the level at which the drag saturates. What has significantly changed, however, are the local fluctuations in surface wave drag. After 125 min of model time, the two simulations display completely different signatures of surface wave drag transience. After surface wave drag saturation, the simulation that employed horizontal spatial filtering displays fluctuations of *greater* amplitude about the level of saturation. In section 3a we discussed how such transience was directly related to the strong pulses of surface wind discovered in the simulation of the 11 January 1972 Boulder windstorm. It appears then, that the drag history of the spatially filtered simulation displays a behavior consistent with the presence of the strong pulses of surface wind discovered in simulations previously presented in this section.

A Hovmöller plot of surface wind is presented in Fig. 24 for the simulation in which horizontal spatial filters were employed. The evolution of surface wind in this and the spatially unfiltered simulation previously presented in section 3c (Fig. 16) appear nearly identical up to 100 min of model time. Subsequent to this time, in the filtered simulation, the Chinook front begins to move downstream with a velocity of 3 m s^{-1}. At 200 min of model time the speed of the front increases abruptly to 7 m s^{-1} and remains very near that value for the remainder of the integration. During this time strong pulses of surface wind appear on the lee slope of the topography and propagate downstream with nearly constant speed to the Chinook front where they abruptly dissipate. These pulses range in phase speed from 20–35 m s^{-1}.

In Fig. 25 five time series and power spectra of surface wind are displayed at distances downstream from the topographic maximum equivalent to those previously presented in Fig. 19 for the unfiltered simulation. A strong transience in surface wind speed develops from the topographic maximum to 30 km downstream. The power spectra of Fig. 25 reveal that these temporal fluctuations are no longer dominated by a single frequency as was found to be the case in section 3c (Fig. 19). At 20 km range, three strong periods of 10.5, 12.6 and 14.3 min are present in the horizontal surface wind.

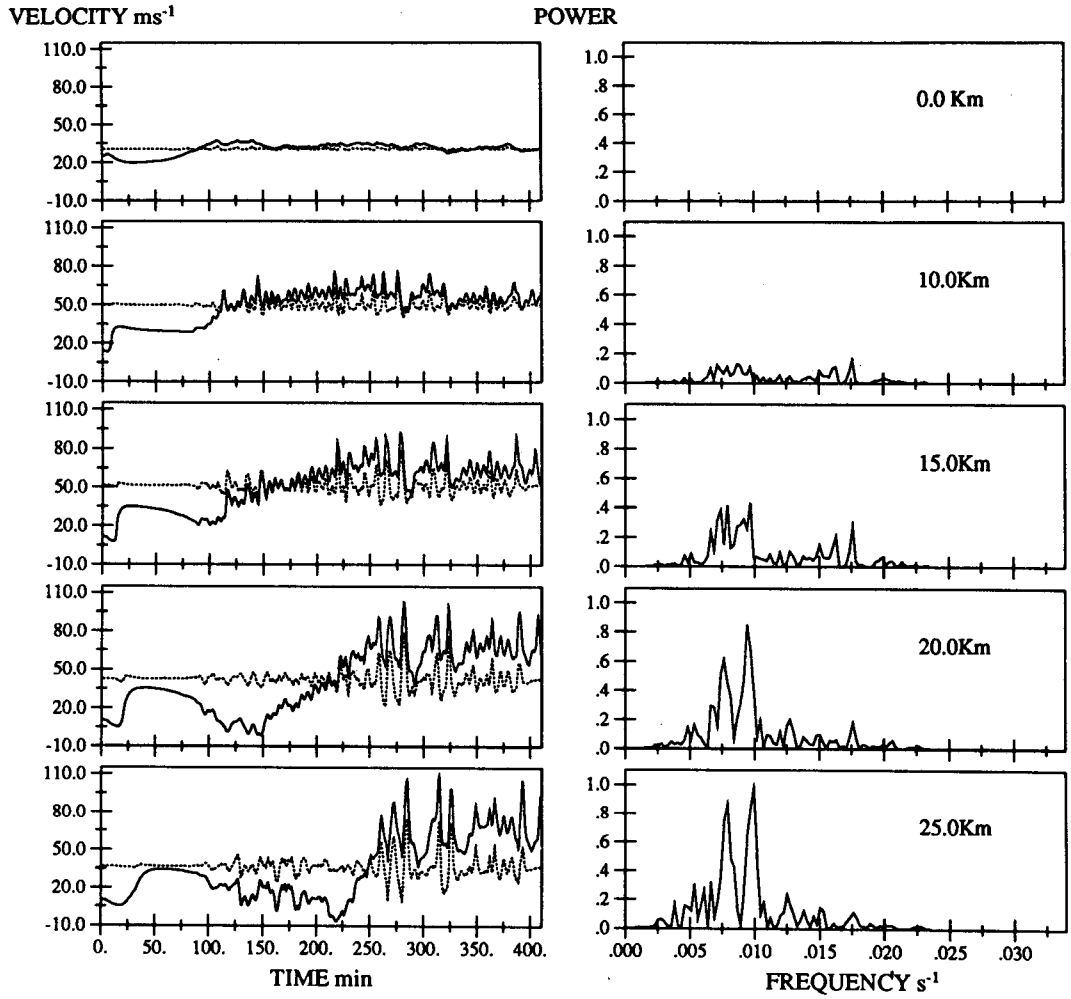

FIG. 22. Time series and associated power spectra of surface wind speed at various positions to the lee of the topography for the modified 11 January profiles incident on a mountain of height $h = 0.935H_J$. Filtered time series (dotted) are displayed as deviations from the mean of the raw time series.

At 30 km downstream, gusts of intensity >125 m s^{-1} occur and the power spectrum reveals dominant 11 and 24 min periodicities.

From these results it is clear that even very strong spatial filtering of high wavenumber structure does not inhibit the occurrence of the pulsation phenomenon. In fact, the simulation that employed strong damping of $2\Delta x$ structure produced pulses of surface wind with maximum wind speeds in excess of those obtained when no damping was employed (section 3c). We may conclude, therefore, that this pulsation phenomenon is not the result of a numerical effect driven by $2\Delta x$ noise.

While the occurrence of the pulsation phenomenon is insensitive to the damping of $2\Delta x$ horizontal structure, it is clear that its detailed characteristics are not. A comparison of the results of this particular subsection and those of section 3c reveal that the phase speed and spatial and temporal periodicity of the pulses of surface wind display significant differences. In order to quantify the strength and effect of the $2\Delta x$ spatial filtering, the temporal evolution of the wavenumber spectrum of the vertical velocity field at elevations of 4, 8 and 12 km were computed over the full horizontal range of the domain for the simulations presented in this subsection and section 3c. The greatest differences were observed to occur at 4 km elevation. In Fig. 26 we present 12 wavenumber spectra calculated at this elevation. These power spectra are displayed at equivalent model times which span the full temporal range of the integrations performed in this subsection (dotted lines) and section 3c (solid lines). The vertical dashed lines in Fig. 26 represent the horizontal wavenumber of the regular pulses of surface wind determined from the simulation presented in section 3c ($\lambda_x \approx 16$ km $= 32\Delta x$).

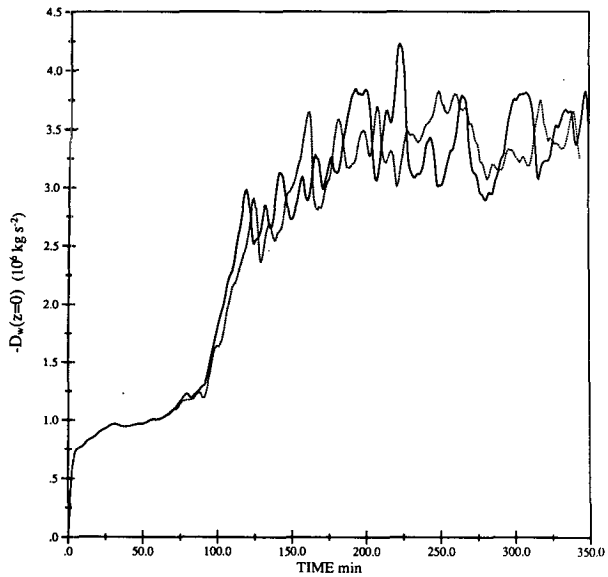

FIG. 23. Surface wave drag history for the modified 11 January 1972 windstorm simulation presented in section 3c with horizontal spatial filtering (solid line) and without horizontal spatial filtering (dotted line).

Initially, at 13.33 min of model time, the two power spectra show slight differences at high wavenumber but appear identical at wavenumbers $< 0.175\Delta x^{-1}$. Significant differences begin to appear at 40.0 min of model time. From wavenumbers of 0.25–$0.5\Delta x^{-1}$ the unfiltered simulation begins to display greater power than the filtered simulation. At 66.67 min, the unfiltered simulation displays an even greater buildup of power at wavenumbers $> 0.35\Delta x^{-1}$. At this time the two power spectra are only identical at wavenumbers $< 0.05\Delta x^{-1}$. At 80.0 min, in the range of 0.1–$0.35\Delta x^{-1}$, the unfiltered simulation delivers power that is approximately one order of magnitude greater than that obtained in the filtered simulation. At higher wavenumber this difference becomes more pronounced.

The power spectra at 106.67 min of model time, however, begin to display a behavior that is consistent with those obtained for the remainder of the integrations. While the detailed distribution of power differs in each simulation, for wavenumbers up to $0.3\Delta x^{-1}$ there is an overlap indicating very little difference in tendency. Due to strong filtering, the power in the filtered simulation at wavenumbers $> 0.3\Delta x^{-1}$ is consistently 1–2 orders of magnitude smaller than that obtained in the unfiltered simulation. This type of behavior was also observed in the temporal evolution of the power spectra calculated from the two simulations at elevations of 8 and 12 km.

At model times near 106.67 min it is important to

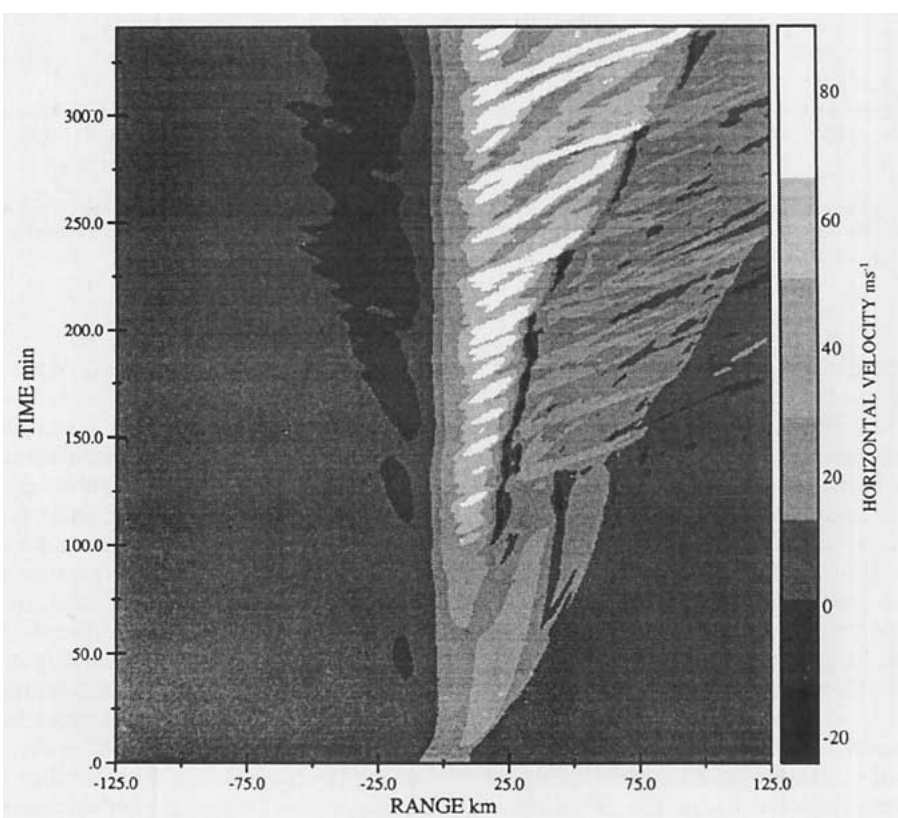

FIG. 24. Hovmöller plot of surface wind for the modified 11 January 1972 windstorm when $2\Delta x$ horizontal spatial filtering is employed.

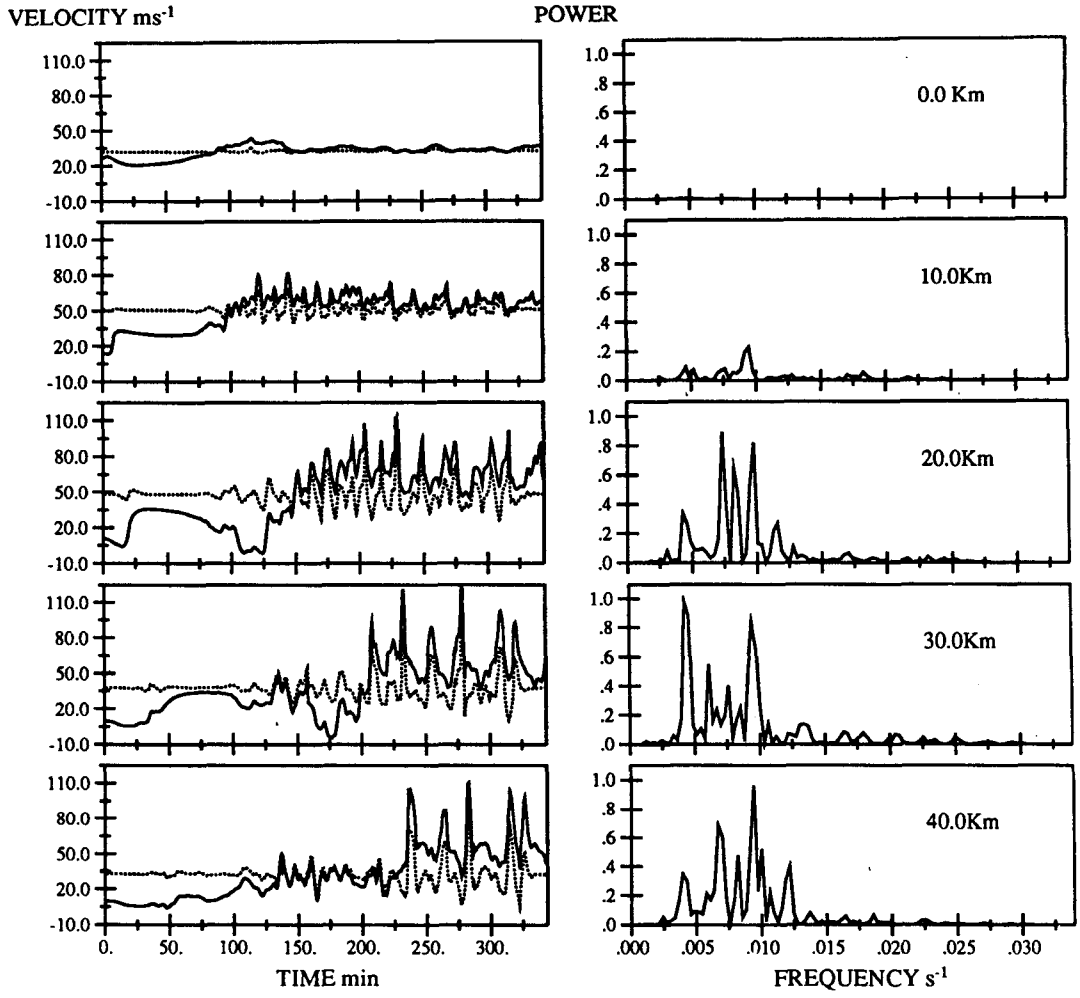

FIG. 25. Time series and associated power spectra of surface wind for the modified 11 January 1972 windstorm simulation when $2\Delta x$ horizontal spatial filtering is employed. These are displayed at ranges downstream of the topographic maximum equivalent to those previously presented in Fig. 19 for the unfiltered simulation.

realize that the pulsation phenomenon had not begun in either simulation (Fig. 16 and Fig. 24). From the above discussion it is clear that the absence of damping of the smaller scale structure of the dependent fields has created a completely different distribution of resolvable background noise prior to the onset of the pulsation phenomenon (Fig. 26, 106.67 min). In fact, the pulses are sensitive to the distribution of noise in the system since, as we will show in a companion paper, the pulses themselves are due to a secondary instability of the mature downslope windstorm flow that is triggered out of the noise present in this background state. As a result, we should expect the detailed nature of the pulses to differ in the filtered and unfiltered simulations of the same storm. This comes as no surprise since we have already demonstrated that the parameters which characterize the pulsation phenomenon are extremely sensitive to slight changes in the upstream incident profiles of horizontal velocity and stability (section 3c) and to small changes in the supercriticality of the flow (section 3d).

4. Conclusions

In this paper we have investigated the ability of two-dimensional numerical simulations of severe downslope windstorms to deliver a transience in surface wind speed that is qualitatively consistent with observational data obtained during actual downslope windstorm events. In our reexamination of the 11 January 1972 Boulder downslope windstorm, we found that an analysis of this phenomenon required a model domain of far greater horizontal and vertical extent than was ever previously employed for its investigation. The extended domain proved essential to adequately represent the flow for the very long time integrations which were necessary because a strong surface transience only developed after the surface wave drag reached saturation. No previous analysis of the formation of severe down-

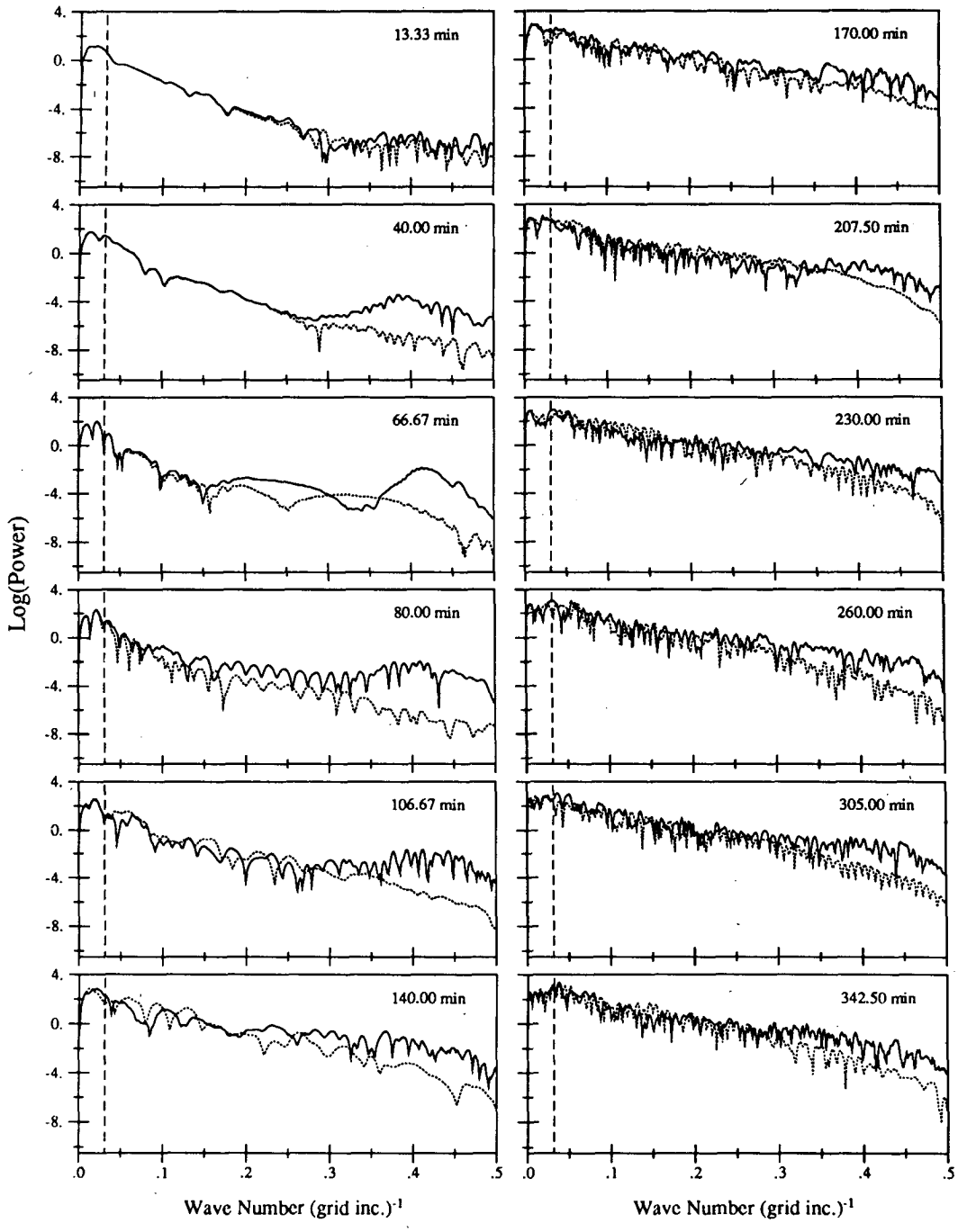

FIG. 26. Temporal evolution of the wavenumber power spectrum of the vertical velocity field at 4 km elevation computed over the full horizontal range of the model domain. The simulation in which horizontal spatial filtering of $2\Delta x$ structure was employed is represented by the dotted lines while the unfiltered simulation is represented by the solid lines. The vertical dashed line in each frame represents the wavenumber of the regular pulses of surface wind determined from the unfiltered simulation presented in section 3c ($\lambda_x \approx 32\Delta x$).

slope windstorms through internal wave breaking has been conducted in which the onset of saturation has been observed and the characteristics of the saturated state systematically investigated. The new extended simulation of this "classic" Boulder event suggests that the 5–15 min quasi-periodic transience in surface wind observed during this event was the result of strong anomalies of horizontal wind that propagate with well-defined phase speed from the lee slope of the topography where they first appear at the surface to the Chinook front where they dissipate. The strength and temporal frequency of these pulses fit quite well the

requirements of the strong 5–15 min fluctuations observed for this storm. The pulsation phenomenon revealed in all of our new simulations also bears a striking resemblance to the transience observed through the recent utilization of pulsed doppler lidar detection techniques during more recent events at Boulder (Neiman et al. 1988).

One of the additional high resolution simulations which we performed, i.e., of the windstorm that developed in a flow with upstream profiles of constant N and U, revealed that in the high drag regime, even these simplest of incident flows give rise to a qualitatively identical pulsation phenomenon in surface wind to the lee of the topographic maximum. Since the occurrence of this surface transience would seem to depend only on whether or not the bifurcation into the downslope windstorm configuration occurs and not on the incident upstream profiles, it is not surprising that the recent observational evidence reported by Neiman et al. (1988) is in qualitative accord with the results of our 11 January 1972 Boulder windstorm simulation even though the two windstorm events are completely distinct.

While the occurrence of the pulsation phenomenon appears to depend only on the evolution of the flow into the downslope windstorm configuration, the precise characteristics of the pulsation appear to be extremely sensitive to the conditions under which the transition is nucleated. When the observed 11 January 1972 upstream soundings of horizontal velocity and temperature were slightly modified, the spatial and temporal regularity of the strong pulses of surface wind were enhanced. When the effect of supercriticality was investigated in section 3d, it was found that a modest 6.5% decrease in the height of the topographic forcing applied to the modified 11 January flow induced a strong modification of the power spectrum of the pulsation. The pulses were no longer regular in space and time and occurred with several rather than a single speed of downstream propagation.

The analyses reported here have all been based upon simplifying assumptions of smooth idealized topography, free-slip lower boundary conditions and two spatial dimensions. These idealizations clearly limit the ability of the simulations to reproduce all of the characteristics of observed downslope windstorm events. In all of our simulations, it was found that the Chinook front propagated continuously downstream after surface wave drag saturation occurred. Observational evidence that would support this behavior has not been reported from studies conducted during actual events. This discrepancy is most probably due to the restriction of the flow to two spatial dimensions (i.e., 2-D topography) and, to some extent, the use of a free-slip lower boundary condition. In physical reality the "active" topography inevitably has some finite extent in the cross-stream direction. When, as in our model simulations, constant upstream forcing is imposed, the air would have the option to flow around rather than over the topography. This extra degree of freedom will clearly act in such a way as to diminish the strength of the storm and inhibit the downstream movement of the Chinook front. Furthermore, Richard et al. (1989) have recently employed a turbulent kinetic energy parameterization in the context of a hydrostatic numerical simulation of the 11 January 1972 event and thereby demonstrated that surface friction may also inhibit the downstream motion of the front.

Because of the simplifying assumptions employed in our model it would seem reasonable to expect that the transience in surface wind observed during an actual downslope windstorm event might be markedly different from that produced in the simulations. Unquestionably, local variations in topography and turbulent boundary layer structure will contribute significantly to the detailed characteristics of the transience in surface wind. The basic pulsation phenomenon discovered in our simulations, however, was found to be both in quantitative and qualitative accord with the O(10 min) quasi-periodic transience observed during actual events even though no account was taken of either of these factors. Since neither a turbulent boundary layer nor higher wavenumber structure in the topography were incorporated into the model, we must conclude that these factors have little to do with the cause of the O(10 min) pulsation phenomenon observed during actual downslope windstorms (Neiman et al. 1988).

The numerical simulations presented in this paper have clearly demonstrated that the downslope windstorm configuration is dynamically unsteady in two spatial dimensions. This result is at odds with the fundamental assumption on the basis of which the three-dimensional simulation of Clark and Farley (1984) was interpreted. Their explanation for the transience observed in this simulation was based upon theory previously proposed by Peltier et al. (1978) and Klaassen and Peltier (1985) in the context of work on the turbulence transition in Kelvin–Helmholtz waves which explained this transition in terms of a shear aligned (3-D) convective instability. In analogy with this theory Clark and Farley suggested that the O(10 min) transience in surface wind whose onset was observed in their numerical simulations was the result of a three-dimensional convective instability of the two dimensional flow. The simulations presented in the present paper, however, reveal that the two-dimensional instability of the flow in the downslope windstorm configuration is itself responsible for producing O(10 min) surface transience that is in close agreement with the most recent detailed observation of this phenomenon (Neiman et al. 1988). Given this evidence, we must therefore conclude that it is quite possible that the transience observed in the Clark and Farley (1984) three-dimensional simulation of the 11 January 1972 Boulder event was actually the onset of the strong two dimensional pulsation discovered in the simulations presented herein.

In a following paper in this new series, we shall investigate the nature of the dynamical mechanism through which these strong pulses of surface wind are generated in the downslope windstorm simulations and, by extension, whenever such severe storms occur in nature. Therein we shall perform a linear stability analysis of the new background states engendered in the lee of the topography during the downslope windstorm simulations presented in this paper. In this investigation we will demonstrate that the pulsations observed in the nonlinear simulations presented in this paper have wavelengths, periods, growth rates and spatial structures consistent with Kelvin–Helmholtz modes of instability predicted to grow exponentially in space from the background states in which the pulses propagate. These results provide convincing evidence that the new mean flow established in the lee of the obstacle by wave mean flow interaction is basically a parallel shear flow. By application of Squire's theorem (Squire 1933), we would then expect that the most unstable modes of the new mean flow would be the two-dimensional modes resolved in the simulations described in the present paper.

If such K–H modes of instability are considered to be responsible for the O(10 min) transience in surface wind, then a reasonable explanation naturally follows for the as yet undiscussed O(1 min) aperiodic velocity fluctuations documented in the anemometer trace previously presented in Fig. 1 for the 11 January 1972 storm. As demonstrated by Klaassen and Peltier (1985), a finite amplitude K–H wave must itself become unstable to a shear aligned convective mode of instability. We expect that the much shorter spatial and temporal scales characteristic of this convective mode might match those observed for the O(1 min) surface transience rather well. We intend to investigate the validity of this hypothesis in future work through fully three-dimensional numerical studies.

Acknowledgments. The computations described in this paper were performed on the CRAY X-MP supercomputer of the Ontario Center for Large Scale Computation at the University of Toronto. CPU time on this machine was made available through the Vector Computer Access program run by the Natural Sciences and Engineering Research Council of Canada. Research support was from NSERC Grant A9627 to W.R.P. and an NSERC Graduate Scholarship to J.F.S.

REFERENCES

Asselin, R., 1972: Frequency filter for time integrations. *Mon. Wea. Rev.*, **100,** 487–490.

Bacmeister, J. T., and R. T. Pierrehumbert, 1988: On high-drag states of nonlinear stratified flow over an obstacle. *J. Atmos. Sci.*, **45,** 63–80.

Clark, T. L., 1977: A small-scale dynamic model using a terrain-following coordinate transformation. *J. Comput. Phys.*, **24,** 186–215.

——, and R. D. Farley, 1984: Severe downslope windstorm calculations in two and three spatial dimensions using anelastic interactive grid nesting: A possible mechanism for gustiness. *J. Atmos. Sci.*, **41,** 329–350.

——, and W. R. Peltier, 1984: Critical level reflection and the resonant growth on nonlinear mountain waves. *J. Atmos. Sci.*, **41,** 3122–3134.

Durran, D. R., 1986: Another look at downslope windstorms. Part I: The development of analogs to supercritical flow in an infinitely deep, continuously stratified fluid. *J. Atmos. Sci.*, **43,** 2527–2543.

——, and J. B. Klemp, 1983: A compressible model for the simulation of moist mountain waves. *Mon. Wea. Rev.*, **111,** 2341–2361.

Gal-Chen, T., and R. C. J. Sommerville, 1975: On the use of a coordinate transformation for the solution of the Navier–Stokes equations. *J. Comput. Phys.*, **17,** 209–228.

Harlow, F. H., and J. E. Welch, 1965: Numerical calculation of time-dependent viscous incompressible flow of fluid with free surface. *Phys. Fluids,* **8,** 2182.

Honika, K. P., 1985: A comparison of numerical simulations of hydrostatic flow over mountains with observations. *Mon. Wea. Rev.*, **113,** 719–735.

Klaassen, G. P., and W. R. Peltier, 1985: The onset of turbulence in finite-amplitude Kelvin–Helmholtz billows. *J. Fluid Mech.*, **155,** 1–35.

Klemp, J. B., and D. K. Lilly, 1975: The dynamics of wave induced downslope winds. *J. Atmos. Sci.*, **32,** 320–339.

Laprise, R. J., and W. R. Peltier, 1989a: The linear stability of nonlinear mountain waves: Implications for the understanding of severe downslope windstorms. *J. Atmos. Sci.*, **46,** 545–564.

——, and ——, 1989b: The structure and energetics of transient eddys in a numerical simulation of breaking mountain waves. *J. Atmos. Sci.*, **46,** 565–585.

Lilly, D. K., 1978: A severe downslope windstorm and aircraft turbulence event induced by a mountain wave. *J. Atmos. Sci.*, **35,** 59–77.

——, and J. B. Zipser, 1972: The front range windstorm of 11 January 1972—a meteorological narrative. *Weatherwise*, **25,** 56–63.

Long, R. R., 1953: Some aspects of the flow of stratified fluids, a theoretical investigation. *Tellus,* **V,** 42–58.

——, 1970: Blocking effects in flow over obstacles. *Tellus,* **22,** 471–479.

Neiman, P. J., R. M. Hardesty, M. A. Shapiro and R. E. Cupp, 1988: Dropper lidar observations of a downslope windstorm. *Mon. Wea. Rev.*, **116,** 2265–2275.

Orlanski, I., 1976: A simple boundary condition for unbounded hyperbolic flows. *J. Comput. Phys.*, **21,** 251.

Peltier, W. R., and T. L. Clark 1979: The evolution and stability of finite-amplitude mountain waves. Part II: Surface drag and severe downslope windstorms. *J. Atmos. Sci.*, **36,** 1498–1529.

——, and ——, 1983: Nonlinear mountain waves in two and three spatial dimensions. *Quart. J. Roy. Meteor. Soc.*, **109,** 527–548.

——, J. Halle and T. L. Clark, 1978: The evolution of finite amplitude Kelvin–Helmholtz billows. *Geophys. Astrophys. Fluid Dyn.* **10,** 53–87.

Pierrehumbert, R. T., and B. Wyman, 1985: Upstream effects of mesoscale mountains. *J. Atmos. Sci.*, **42,** 977–1003.

Richard, E., P. Mascart and E. C. Nickerson, 1989: On the role of surface friction in downslope windstorms. *J. Appl. Meteor.*, in press.

Robert, A. J., 1966: The integration of a low order spectral form of the primative meteorological equations. *J. Meteor. Soc. Japan.*, **44,** 237–245.

Simard, A., and W. R. Peltier, 1982: Ship waves in the lee of isolated topography. *J. Atmos. Sci.*, **39,** 587–609.

Smith, R. B., 1977: The steepening of hydrostatic mountain waves. *J. Atmos. Sci.*, **34,** 1634–1654.

Squire, H. B., 1933: On the stability of three-dimensional disturbances of viscous flow between parallel walls. *Proc. Roy. Soc. London,* **A142,** 621–628.

Yih, C. S., 1960: Exact solutions for steady two-dimensional flow of a stratified fluid. *J. Fluid Mech.*, **9,** 161–174.